Available online at www.sciencedirect.com

ScienceDirect

Geochimica et Cosmochimica Acta 332 (2022) 57–77

Geochimica et Cosmochimica Acta

www.elsevier.com/locate/gca

Soil potassium isotope composition during four million years of ecosystem development in Hawai'i

Wenshuai Li [a,b], Xiao-Ming Liu [a,*], Kun Wang [c], Yoshio Takahashi [b], Yongfeng Hu [d], Oliver A. Chadwick [e]

[a] Department of Earth, Marine and Environmental Sciences, University of North Carolina, Chapel Hill, NC, USA
[b] Department of Earth and Planetary Science, Graduate School of Sciences, University of Tokyo, Tokyo 113-0033, Japan
[c] Department of Earth and Planetary Sciences and McDonnell Center for the Space Sciences, Washington University in St. Louis, MO 63130, USA
[d] Canadian Light Source, University of Saskatchewan, Saskatoon, Canada
[e] Department of Geography, University of California, Santa Barbara, CA, USA

Received 7 April 2021; accepted in revised form 20 June 2022; Available online 24 June 2022

Abstract

We combine spectroscopic and geochemical approaches to interpret the fate of potassium (K) during forest soil development along a 4-million-year chronosequence sampled from relatively undisturbed rainforests in Hawai'i. Potassium derived from weathering of lava is dominant in the youngest site (0.3 ky), but its contribution to the soil K budget declines as weathering progresses. Sites older than 0.3 ky are characterized by substantial K depletion ($\tau_{K,Nb} \sim -1$), with soil isotopic composition ($^{41}K/^{39}K$, $\delta^{41}K$) varying from $-1.91 \pm 0.08‰$ to $-0.09 \pm 0.08‰$, relative to the homogeneous basaltic substrate ($-0.48‰$). Exchangeable and interlayered K show $\delta^{41}K$ values ranging from $-1.32 \pm 0.06‰$ to $0.06 \pm 0.08‰$, higher than their corresponding bulk $\delta^{41}K$ values. The $\delta^{41}K$ patterns of soils and exchangeable components are vertically similar, implying similar environmental controls. The variability in K phase and isotope composition reflects the accumulative effect of different processes. Chemical weathering and plant cycling retain isotopically light K in soils, in particular for 20–150 ky sites. In contrast, atmospheric inputs of marine aerosols (0.14‰) and mineral aerosols ($-0.44‰$) add heavier K (than native basalts) and crust-like K (similar to basaltic $\delta^{41}K$) in soils, respectively. In sites older than 150 ky, nearly complete depletion of basaltic K and reduced plant K imprints result in the dominance of atmospheric inputs in soils. In sum, this study emphasizes the sensitivity of $\delta^{41}K$ to terrestrial biotic and abiotic K cycles.

Keywords: Weathering; Basalt; Aerosol; Chronosequence; Biogeochemistry; XANES

1. INTRODUCTION

Potassium is an essential nutrient in terrestrial ecosystems (Tripler et al., 2006; Sardans and Peñuelas, 2015). At Earth's surface, K is released to the hydrosphere by weathering and microbial solubilization of organic matter; K in solutions can be taken up by organisms or leached into groundwater and rivers (Arnold, 1960; Lenton and von Bloh, 2001; Lucas, 2001; Han and Lee, 2005; Tripler

Abbreviations: XANES, X-ray absorption near-edge structure; MAP, mean annual precipitation; SRO, short-order-range; NH_4Ac, ammonium acetate; $NaBph_4$, sodium tetraphenylborate; NH_4Ox, ammonium oxalate; UCC, Upper Continental Crust

* Corresponding author.
E-mail address: xiaomliu@unc.edu (X.-M. Liu).

https://doi.org/10.1016/j.gca.2022.06.025
0016-7037/

et al., 2006). Although K is very soluble, it is retained in the soil–plant system by both biotic and abiotic processes (Sardans and Peñuelas, 2015). With analytical advances in MC-ICP-MS (e.g., Li et al., 2016; Hu et al., 2018; Morgan et al., 2018; Chen et al., 2019; Li et al., 2020b; An et al., 2022; Zheng et al., 2022), stable K isotopes can now be used to probe the complex sources and cycles of ecosystem K.

The K isotope ratio ($^{41}K/^{39}K$, denoted as $\delta^{41}K$) of K reservoirs on Earth's surface has been characterized, enabling the use of stable K isotopes in tracing K source mixing. Recent studies reached a reasonable estimate of homogeneous $\delta^{41}K$ value for the Bulk Silicate Earth and modern seawater of $-0.48 \pm 0.03‰$ (Wang and Jacobsen, 2016) and $0.14 \pm 0.02‰$ (Hille et al., 2019; Wang et al., 2020), respectively. By contrast, the upper continental crust (UCC, a sum of diorite, granodiorite, graywacke, pelite, granite, loess, shale and tillite, etc.) displays heterogeneous isotopic compositions from -0.68 to $-0.12‰$, with an average $\delta^{41}K$ value of $-0.44 \pm 0.05‰$ (Huang et al., 2020). Recent studies reported wide variations in the direction and magnitude of changes in K isotope composition driven by fluid-rock interaction and biogeochemical cycling of K. Recent studies on regolith, river water, and sediments suggested that there is preferential partitioning of isotopically lighter K into clay minerals compared with their parent sources, to balance the heavier K isotope compositions in riverine dissolved loads and modern seawater (Li et al., 2019; Chen et al., 2020; Teng et al., 2020; Santiago Ramos et al., 2020; Wang et al., 2021).

The direction and magnitude of K isotope fractionation depend on environmental factors. For example, experiments have demonstrated that ^{41}K is preferentially adsorbed on clay surfaces while ^{39}K tends to accumulate into the clay structure (Li et al., 2021a). Field and greenhouse-based studies confirm plant preference for ^{39}K, with plant-mediated isotopic fractionation of as much as $\sim 2‰$ (Christensen et al. 2018; Li et al., 2021b). Chaudhuri et al. (2007) estimated 40–70% of dissolved K in global rivers was affected by plant cycling based on differences in the K/Rb ratios of rock materials, plants, and waters. By contrast, Wang et al. (2021) suggested that high K/Rb ratios and $\delta^{41}K$ values in river water were primarily affected by incongruent weathering. These uncertainties call for further studies on comparative contributions of chemical weathering and biological cycling to K isotope records. Few studies illustrated the correlation between K chemical interactions and K isotope compositions in the regolith with clear geological and ecological contexts. Some studies avoided biologically perturbed soils during sampling for simplicity (Chen et al., 2020; Teng et al., 2020). Considering its biological importance, it is critical to understand the fate of K in terrestrial ecosystems (Sardans and Peñuelas, 2015), and K isotopes will help to address this. So far, there is a scarcity of knowledge of K isotope variation related to K phase partitioning in biologically active soil environments.

The Hawaiian Islands serve as a model system to evaluate the patterns and causes of soil biogeochemical variations because they can be more easily characterized than many continental systems with respect to past and present climate and the organisms they support, as well as maintaining relatively constant topography and substrate materials (Vitousek, 2004). Hence, the changing sources and fates of nutritive elements across the Hawaiian Islands have been extensively investigated along environmental gradients (e.g., annual rainfall and substrate age) (Chadwick et al., 1999; Wiegand et al., 2005; Chadwick et al., 2007; Thompson et al., 2007; Bullen and Chadwick, 2016; Helfenstein et al., 2018). In particular, by matching elevation, rainfall, slope position, and disturbance history, it is possible to put together a sequence of soils that varies principally in the substrate age (Crews et al., 1995). The resulting chronosequence provides insights into the elemental budget modulated by chemical weathering, biological cycling, and exogenous inputs (i.e., dust and marine aerosols without any anthropogenic perturbation) over time (Vitousek et al., 1997; Kennedy et al., 1998; Chadwick et al., 1999; Kurtz et al., 2001; Vitousek, 2004).

This study focuses on linking soil K isotope signals with the source mixing and elemental partitioning during humid forest ecosystem development in Hawai'i. Here, we report the K isotope compositions of bulk soils and chemical extracts from soils on Hawaiian shield volcanoes of the following ages: 0.3, 20, 150, 1,400, and 4,100 ky. The mean annual rainfall for each site is ~2500 mm/yr and the mean annual temperature is ~16 °C (Vitousek, 2004). The objectives of this study are to (i) evaluate the mechanisms and comparative contributions of environmental factors on soil K isotope composition, and (ii) determine the phase partitioning and isotopic variation of K during a 4-million-year history of ecosystem development. Our study provides new insights into soil K isotope variations produced by time-dependent changes in basalt weathering, biological cycling, and atmospheric inputs.

2. GEOLOGICAL BACKGROUND

The soil samples analyzed come from a well-characterized chronosequence located on the Hawaiian Islands where soil sampling sites were established based on the following criteria (Crews et al., 1995; Chadwick et al., 1999; Vitousek et al., 1999; Vitousek, 2004): (1) stable shield surfaces primarily composed of tholeiitic or alkalic lava flows augmented by the surface deposition of tephra (collectively called "basaltic substrate" in this paper), (2) soil substrate ages of about 0.3 ky (Ola'a), 20 ky (Laupāhoehoe), 150 ky (Kohala), 1,400 ky (Moloka'i) and 4,100 ky (Kaua'i), (3) 1,200 m elevation to maintain a common present-day temperature, (4) present-day MAP of ~2,500 mm/yr, and (5) relatively undisturbed montane forests dominated by 'ōhi'a trees (*Metrosideros polymorpha* Gaudich., Lynch et al., 2012) (Fig. 1).

At each sampling site, soils were described using standard terminology (Soil Survey Staff, 2017) and collected by horizon from surface to >1 m in depth except at the youngest site where weathering is not evident at >80 cm depth. The chronosequence is interpreted as a developmental sequence whereby the oldest soil has passed through all the stages (soil properties) represented by the younger sites (e.g., Vitousek et al., 1997; Vitousek, 2004). As soil profiles

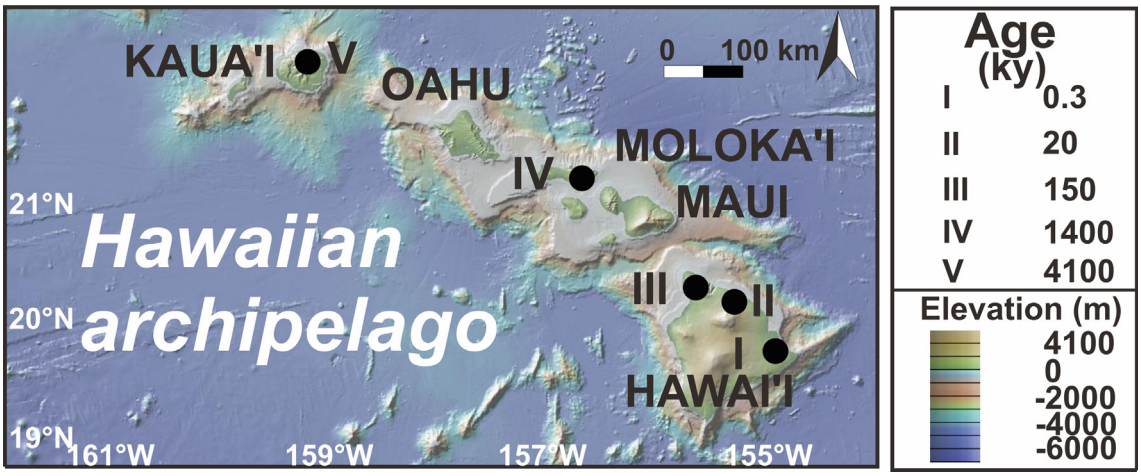

Fig. 1. Location of chronosequence in the Hawaiian archipelago (map produced by GeoMap App, https://www.geomapapp.org/MSInstall.html). The chronosequence soils here vary in ages of 0.3–4,100 ky and have been referred to as the "Long-Substrate Age Gradient (LSAG)" (Vitousek et al., 1997). Soils were sampled from primary shield volcano surfaces to minimize the effects of physical erosion and/or local redistribution of soil solutions.

are open chemical and physical systems, they can be influenced by erosion, weathering of the basalt substrate and exogenous deposition of minerals and soluble ions. In Hawai'i, atmospheric deposition of mineral aerosols and marine aerosols become critical determinants of soil chemistry since basaltic phases are largely depleted by weathering (e.g., Kennedy et al., 1998; Chadwick et al., 1999; Vitousek et al., 1999; Kurtz et al., 2001; Chadwick et al., 2009). This chronosequence interpretation assumes constant climatic conditions – an assumption that is seldom met in reality. The Hawai'i chronosequence covers from the present interglacial back through the Pleistocene and into the Pliocene period and therefore has been influenced by dramatically different global climate regimes. Against this backdrop, local climate change has been buffered by the near-tropical marine setting, by the interaction of the northeast trade winds over time, and by the fact that the trade winds interacted with long-lived topographic features of the individual volcanoes (Hotchkiss et al., 2000). Although detailed climate differences for each site cannot be fully reconstructed, climate fluctuation was modeled in Hotchkiss et al. (2000). The work by Hotchkiss et al. (2000) showed that eustatic sea-level changes and variations in the altitude of tropical inversion layers likely induced short term climate fluctuations, causing some of the sites to be drier during the last glacial maximum event (Hotchkiss et al., 2000).

Over the long timescale represented by the volcanoes of Hawai'i, this chronosequence shows rapid weathering of primary minerals and depletion of alkali and alkaline earth ions followed by longer-term losses of silicon and aluminum (Ziegler et al. 2005; Chadwick et al., 2020). Such a change leads to the decline in the acid-neutralizing capacity and subsoil pH (1:1v/v H_2O-to-soil) that varied from circumneutral in the youngest site to weakly acidic (pH ~4) in the older sites (Table 1) (Chadwick and Chorover, 2001). The youngest site of 0.3 ky is classified as Andisols (Soil Survey Staff, 2017) dominated by primary basaltic materials. Early weathering of the basaltic substrate promotes the development of non-crystalline secondary minerals followed by slow ripening of crystalline secondary minerals such as halloysite, gibbsite, hematite, and goethite (Kennedy et al., 1998; Vitousek et al., 1999; Chadwick and Chorover, 2001; Chorover et al., 2004; Ziegler et al., 2005) (Fig. 2a). Three intermediate-aged soils (20, 150, and 1,400 ky) are classified as more weathered Andisols enriched in metastable secondary phases, whereas the oldest soil (4,100 ky) is classified as an Oxisol dominated by inert crystalline Al/Fe-oxides and kaolin (Vitousek et al., 1997; Chorover et al., 2004).

Montane forest productivities were estimated by the tree basal area (Wardle et al., 2004, Fig. S1). Net primary productivity reaches a maximum at the 20 ky site and gradually declines in the older sites (Vitousek, 2004). The 150 ky site is located on the Hāwī lavas that are alkalic in nature (Crews et al., 1995; Spengler and Garcia, 1988). Hence, it could inherit higher K concentrations than occurred in other chronosequence soils. In addition, the 150 ky site has the highest content of mica/illite delivered to the soil by long-distance transport of mineral aerosols (Chadwick et al., 1999; Kurtz et al., 2001; Vitousek, 2004). In sites over 150 ky, the quartz/mica ratio of mineral aerosol-derived soil mass increases, which implies more intense weathering of micaceous minerals in more depleted soils (Kurtz et al. 2001). Based on Nd and Sr isotope data in Kurtz et al. (2001), Arendt et al. (2015) quantified the contributions of marine aerosols and mineral aerosols, and native basaltic sources (Fig. 2b) in depth and over time. Based on model outputs, the imprints of mineral aerosols are important in the 150 ky site at depth <30 cm and the contribution of marine aerosols is significant at shallow soil layers except for the 0.3 ky site. Native basaltic contribution is important in the youngest site. It was suggested that radiogenic isotopes such as $^{87}Sr/^{86}Sr$ can be used to trace not only the fate of Sr and Ca, but also macronutrients such as K, Mg, and P

Table 1
Physicochemical and mineralogical characterization of Hawaiian chronosequence soils.

Horizons	Depth cm	Organic carbon %	pH 1:1 H_2O	SRO mineral %	Fe hydroxides %	Halloysite[1] + Gibbsite %	Kaolin (halloysite) %	Quartz %	Mica/illite %	Feldspar %	Other %
Ola'a 0.3 ky											
OL1	0–3	36.9	4.1	9.4	2.8	10.5	0.1	0.1	0.9	6.1	70.1
OL2	3–8	13.1	5.2	7.8	3.3	6.1	0.2	0.1	1.8	11.2	69.5
OL3	8–13	8.4	5.3	9.5	3.8	5.0	0.2	0.0	1.9	15.8	63.8
OL4	13–21	3.9	5.7	10.9	4.2	5.0	0.1	0.0	1.9	14.1	63.8
OL5	21–27	3.5	5.7	14.1	5.0	9.1	0.1	0.0	1.6	14.0	56.1
OL6	27–36	1.0	6.3	17.9	5.0	7.4	0.2	0.0	1.4	12.8	55.3
OL7	36–45	0.3	6.6	14.4	5.9	7.8	0.5	0.0	1.7	13.5	56.2
OL8	45–64	0.1	6.8	8.7	5.4	9.7	0.4	0.0	1.9	18.1	55.8
OL9	64–79	0.1	6.9	7.2	5.6	12.7	0.5	0.0	2.1	17.7	54.2
Laupāhoehoe 20 ky											
LA1	0–5	55.6	3.7	4.2	1.3	12.9	0.1	0.5	0.2	0.0	80.8
LA2	5–12	32.4	3.7	14.2	19.2	5.4	0.3	1.9	1.3	0.0	57.7
LA3	12–20	13.9	4	27.1	9.5	3.6	0.2	2.4	1.3	0.0	55.9
LA4	20–27	10.0	4.7	18.6	38.9	3.2	0.5	4.9	2.1	0.0	31.8
LA5	27–39	10.9	4.7	34.5	13.3	5.8	0.5	5.9	4.7	1.9	33.4
LA6	39–52	5.9	4.8	0.0	44.5	5.8	0.9	3.7	1.6	0.0	18.9
LA7	52–71	10.0	4.9	50.1	11.7	3.3	0.3	1.6	1.0	0.2	31.8
LA8	71–94	10.0	5.0	54.7	10.2	4.2	0.4	2.5	2.2	0.2	25.6
Kohala 150 ky											
KO1	0–4	38.9	4.2	3.9	2.4	7.2	0.9	10.9	5.4	0.2	69.1
KO2	4–11	27.5	3.9	7.1	3.4	4.9	1.8	21.6	11.0	0.4	49.8
KO3	11–21	20.0	4.1	4.4	4.1	4.5	2.2	32.8	17.7	0.4	33.9
KO4	21–30	16.0	4.3	32.7	3.1	7.1	1.2	7.7	5.1	0.1	43.0
KO5	30–48	10.3	4.9	43.9	2.3	35.1	0.2	1.1	1.1	0.1	16.2
KO6	48–66	9.2	5.1	33.6	2.5	46.3	0.3	1.2	0.8	0.2	15.1
KO7	66–78	8.1	5.1	55.1	2.4	34.1	0.2	0.9	0.3	0.2	6.8
KO8	78–89	8.4	5.1	31.1	1.7	49.4	0.5	2.3	1.1	0.0	13.9
KO9	89–98	7.3	4.9	35.7	6.8	48.4	0.3	0.3	0.6	0.0	7.9
Moloka'i 1,400 ky											
MO1	0–4	33.0	4.2	0.9	0.5	6.9	0.5	8.0	0.3	0.0	82.8
MO2	4–7	10.1	3.9	13.0	6.5	15.5	4.5	11.8	5.3	1.6	41.8
MO3	7–14	8.5	4.0	13.2	5.8	13.7	6.3	14.2	5.7	0.3	40.8
MO4	14–23	5.7	4.3	14.7	7.6	20.6	5.8	11.7	5.1	0.2	34.3
MO5	23–38	4.7	4.6	14.0	8.0	17.0	8.0	13.5	4.5	0.2	34.8
MO6	38–58	3.9	4.9	25.8	7.9	30.9	11.8	1.1	1.5	0.1	20.9
MO7	58–78	1.4	5.1	23.4	7.7	35.8	14.7	1.0	1.1	0.1	16.2
MO8	78–100	2.4	5.1	21.0	5.6	35.9	18.3	1.1	0.9	0.2	17.0
Kaua'i 4,100 ky											
KA1	0–5	32.9	4.1	3.5	1.7	5.5	0.3	10.0	0.3	0.0	78.7

KA2	5–11	17.6	3.8	4.6	2.8	3.4	0.3	14.5	0.4	0.0	74.0
KA3	11–16	13.5	4.0	2.8	41.5	5.1	0.7	11.8	0.4	0.0	37.7
KA4	16–23	5.3	4.3	4.0	25.9	7.8	1.2	22.1	0.8	0.0	38.2
KA5	23–32	5.8	4.4	6.4	49.0	12.6	5.5	3.1	2.2	0.0	21.2
KA6	32–43	4.2	4.7	4.4	42.9	24.3	9.4	4.0	1.0	0.0	14.0
KA7	43–54	5.6	4.8	4.8	37.2	22.4	14.1	0.3	0.5	0.0	20.7
KA8	54–72	1.7	4.9	5.1	34.9	24.8	17.8	0.2	0.4	0.0	16.8
KA9	72–89	1.2	4.9	5.3	29.9	28.9	18.2	0.0	0.4	0.0	17.3
KA10	89–100	1.3	5.1	5.1	25.7	28.2	20.6	0.0	0.4	0.0	20.0

Note: Presented data are mean values of duplicate samples. Soil organic carbon was measured by TOC analyzer (IR. Detector). Soil pH is measured by a 1:1 v/v mix of soil and Milli-Q water (Bargrizan et al., 2017). SRO minerals: short-range-order minerals. Mineralogy is determined by XRD Rietveld refinement. Other represents "primary silicate phases".

[1] Poorly crystalline halloysite.

(Uhlig et al., 2020). Finally, the applicability of using Nd-Sr isotopes for tracing K cycles is assessed in this study.

3. ANALYTICAL METHODS

3.1. Mineralogy analysis

XRD patterns were obtained in a 2θ range from 5° to 60° with a step interval of 0.02° and a scan rate of 0.5°/min (Fig. S2). Methods of mineralogical identification have been given in Chorover et al. (1999) and the results are provided in Table 1.

3.2. Chemical extraction

Soils were extracted using different chemical regents to separate various compartments. We note that the extraction steps using ammonium acetate (NH_4Ac), ammonium oxalate (NH_4Ox), and hydrogen peroxide (H_2O_2) were performed in parallel. The extraction using sodium tetraphenyl borate ($NaBPh_4$) was performed after NH_4Ac treatment of the same sample. A brief description of the processes and implications of experiments are given below.

Soil exchangeable K (bioavailable K) was extracted using 1 M ammonium acetate (NH_4Ac) buffered at a pH of 7 (Table 2). Soil organic-associated K may be partially extracted using NH_4Ac due to possible decomposition of organic matter by the treatment thus releasing internally bound K. After NH_4AC extraction, interlayered K in mica minerals was extracted using sodium tetra-phenyl borate ($NaBPh_4$) solutions (a mixture of 0.25 mol/L $NaBPh_4$ + 1.7 mol/L NaCl + 0.01 mol/L EDTA, Cox et al.,1999).

To quantify the K fraction associated with soil organic matter, we used a standardized chemical extraction method (Community Bureau of Reference, BCR). Soil K in oxidizable fraction (defined as sulfides and organic matters) was extracted using 30% H_2O_2 + 0.11 M CH_3COONH_4 (1:20 w/v ratio) to estimate the amount of organic-K in the total soil K pool.

To estimate the fraction of total extractable K, soils were also extracted using a mixture of 0.2 M ammonium oxalate (NH_4Ox) and 0.2 M oxalic acid at pH = 3 (1:100 w/v ratio), following the method in Blakemore (1987). Not only short-ranger-order (SRO) phases but also humus-ions could be removed (Soil Survey Laboratory Staff, 2004). Data of organic-K are compared to justify the selection of the humic-K spectrum in section 3.5. Only the top five soil samples of each site were extracted using H_2O_2 and NH_4Ox.

3.3. Elemental analysis

To obtain refined compositional descriptions of major elements, soils were analyzed using X-ray fluorescence (XRF) at the ALS Chemex Labs following a $Li_2B_4O_7$ fusion protocol. Oxide data by XRF was used to calculate the chemical index of alteration (CIA) (Table 2).

After weighing, ~50 mg samples were transferred into Teflon® vessels and dissolved in a mixture of concentrated

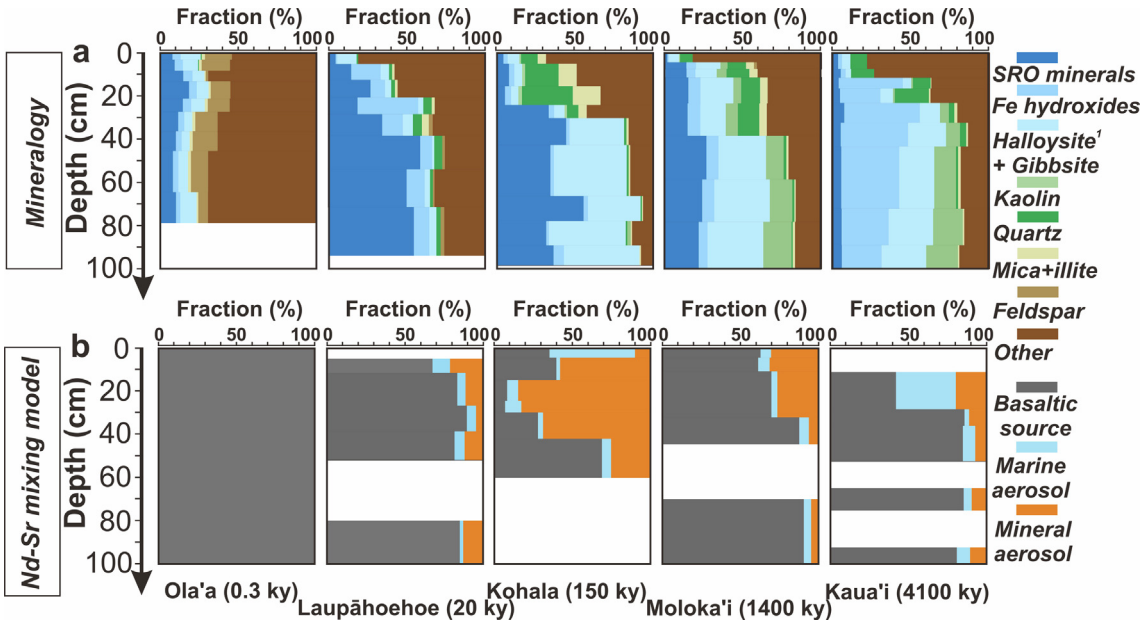

Fig. 2. Vertical profiles of (a) mineralogy (XRD in Fig. S2, Table 1, soil mineralogical composition refer to Kurtz et al., 2001), and (b) soil source mixing pattern based on Nd-Sr isotope models (basaltic substrate, marine aerosols, and mineral aerosols derived from the Bayesian Monte-Carlo simulation (data from Arendt et al., 2015) in soil sites along the chronosequence. Numerical XRD data are provided in the SI.

$HCl + HNO_3 + HF$ over 120 °C. Digested samples were dried and redissolved in 0.05 N HCl in a thermostatic oven at 60 °C over a week and transferred to a hotplate at 120 °C until complete dissolution. After evaporation, digested samples were refluxed using 2 mL 2% HNO_3. The concentrations of Li, Na, K, Mg, Al, Fe, Ca, Sr, and Ti were measured on a Q-ICP-MS (Agilent™ 7900) at University of North Carolina, Chapel Hill, and the results are listed in Table 2. Internal standards of Be, Ge, Rh, In, Ir, and Bi were used for corrections. Standards BHVO-2 (basalt) and SBC-1 (shale) were used to evaluate the analytical accuracy, which was <10% (2 S.D.) for all elements (Table S1). The data of Q-ICP-MS were used to determine soil K concentration and K loss/gain.

The relative K gain ($\tau_{K,Nb} > 0$) or loss ($\tau_{K,Nb} < 0$) in the <2-mm soil fraction for each soil-depth profile was estimated as follows (Brimhall and Dietrich, 1987; Chadwick et al., 1990): $\tau_{j,w} = (C_{j,w} \times C_{i,p})/(C_{j,p} \times C_{i,w}) - 1$, where C is the concentration of an element of interest, w and p are weathered, and parent materials, respectively, and i and j notate the immobile and mobile elements, respectively. Kurtz et al. (2000) concluded that Nb is the least mobile element in Hawaiian soils; therefore we used Nb for the tau (τ) calculations.

3.4. Potassium isotope analysis

All chemical procedures were conducted in a laminar flow hood (class-100) (Airclean™, 600 PCR). Samples were processed with ultra-pure, double-distilled reagents. An aliquot of digested sample was evaporated to dryness at 120 °C, and then dissolved in 2 mL 0.7 M HNO_3 for ion-exchange separation and purification of K. The K isolation from matrices was performed following the method in Chen et al. (2019). In brief, a two-step procedure was applied to separate K from other matrix elements, including the first column (inside diameter, ID = 1.5 cm, Bio-Rad™, AG50-X8, 200–400 mesh, resin volume of 17 mL) and the second column (ID = 0.5 cm, Bio-Rad™, AG50-X8, 200–400 mesh, resin volume of 2.4 mL). Loaded resin was precleaned and conditioned in 0.7 M and 0.5 M HNO_3 for the first and second columns, respectively.

Potassium isotope analyses were performed using the MC-ICP-MS (Thermo Scientific™, Neptune Plus) at the Isotope Cosmochemistry Laboratory, Washington University in St. Louis. We used cold plasma to suppress interferences from residual and isobaric ($^{40}Ar^1H^+$ on $^{41}K^+$ and $^{38}Ar^1H^+$ on $^{39}K^+$) argides (Chen et al., 2019). In addition to monitoring $^{41}K/^{39}K$ ratios, possible isobaric interference of $^{40}CaH^+$ was monitored by measuring the intensity of the $^{44}Ca^+$ peak. Diluted K-bearing solution (5–8 mg/L, 3 % HNO_3) was introduced in the instrument by Elemental Scientific™ APEX omega nebulizer, equipped with a desolvation membrane to improve sensitivity and reduce hydride and oxide generation. Instrumental mass fractionation was corrected using the sample-standard bracketing protocol and the sample-standard cycle was repeated with n sessions ($n \geq 5$). Details of the instrumentation were given in Chen et al. (2019). The K isotope compositions are reported in a δ-notation ($\delta^{41}K$), as parts per thousand (‰) deviation from the NIST SRM 3141a (Teng et al., 2017):

$$\delta^{41}K\ (‰) = \left\{ \frac{(^{41}K/^{39}K)_{sample}}{(^{41}K/^{39}K)_{NIST\ SRM\ 3141a}} - 1 \right\} \times 1000 \qquad (1)$$

Both two standard deviation (2S.D.) and 95% confidence interval (95% c.i.) were provided in Table S2 and we used 95% c.i. as the analytical error in the plots.

Table 2
Elemental characterization of Hawaiian chronosequence soils.

Horizons	Depth cm	SiO_2 wt.%	Al_2O_3 wt.%	Fe_2O_3 wt.%	CaO wt.%	K_2O wt.%	CIA	[K] g/kg	NH_4Ac-K g/kg	NH_4Ox-K g/kg	Organic-K g/kg	$\tau_{K, Nb}$	K/Rb molar
Ola'a 0.3 ky													
OL1	0–3	13.3	3.0	3.5	2.7	0.2	33.8	1.5	0.7	1.3	0.6	−0.07	959.4
OL2	3–8	31.4	8.9	9.9	6.1	0.2	40.1	1.9	0.3	0.8	0.4	0.00	1019.0
OL3	8–13	42.0	11.2	11.6	8.2	0.3	38.5	2.6	0.1	0.7	0.1	−0.07	1121.2
OL4	13–21	42.1	12.1	11.8	8.1	0.3	40.7	2.1	0.0	0.7	0.1	0.00	1105.1
OL5	21–27	44.8	12.3	12.5	8.4	0.3	40.1	2.3	0.0	0.8	0.1	−0.04	1207.1
OL6	27–36	47.1	12.8	12.9	9.1	0.3	39.1	2.3	0.0			−0.05	1157.6
OL7	36–45	47.8	12.8	12.6	9.1	0.3	39.3	2.4	0.0			−0.03	1184.3
OL8	45–64	50.3	12.3	12.3	9.7	0.3	36.8	3.4	0.0			0.21	1197.2
OL9	64–79	50.3	12.3	12.3	9.7	0.4	36.9	2.6	0.0			0.09	1156.1
Laupāhoehoe 20 ky													
LA1	0–5	2.0	1.3	4.8	0.2	0.1	72.4	0.7	0.6	0.6	0.6	−0.84	285.5
LA2	5–12	5.4	3.0	30.5	0.2	0.1	85.1	1.1	0.2	0.3	0.2	−0.86	156.6
LA3	12–20	5.0	5.1	32.4	0.3	0.1	87.1	0.9	0.1	0.2	0.1	−0.96	702.3
LA4	20–27	9.2	11.0	35.1	0.1	0.2	95.2	1.3	0.1	0.2	0.1	−0.92	417.2
LA5	27–39	19.8	17.3	22.4	1.4	0.5	83.7	3.1	0.0	0.0	0.0	−0.80	866.5
LA6	39–52	6.7	11.2	38.8	0.0	0.2	98.2	1.0	0.0			−0.94	370.2
LA7	52–71	9.4	21.4	22.7	0.1	0.1	98.2	0.6	0.0			−0.94	296.2
LA8	71–94	12.2	21.7	21.4	0.1	0.3	97.9	1.2	0.0			−0.79	318.0
Kohala 150 ky													
KO1	0–4	17.1	6.2	4.2	0.1	0.6	86.4	4.2	0.4	1.3	1.0	−0.84	450.0
KO2	4–11	31.8	10.0	8.7	0.1	1.1	86.8	7.2	0.1	0.3	0.4	−0.87	424.9
KO3	11–21	45.8	13.5	9.5	0.0	1.5	84.2	13.4	0.0	0.8	0.5	−0.91	294.2
KO4	21–30	17.3	21.7	7.8	0.1	0.5	96.5	2.7	0.0	0.5	0.0	−0.93	382.1
KO5	30–48	12.9	34.0	2.8	0.1	0.2	98.8	0.6	0.0	0.1	0.0	−0.97	376.4
KO6	48–66	14.3	34.9	3.4	0.0	0.0	99.1	0.5	0.0			−0.98	423.1
KO7	66–78	13.7	36.1	1.9	0.0	0.1	99.5	0.2	0.0			−0.99	497.6
KO8	78–89	13.5	26.5	3.8	0.0	0.0	99.4	0.4	0.0			−0.94	435.6
KO9	89–98	n.d.	n.d.	n.d.	n.d.	n.d.	n.d.	0.4	0.0			−0.98	528.7
Moloka'i 1,400 ky													
MO1	0–4	4.6	2.1	1.5	0.2	0.1	84.1	0.8	0.4	0.4	0.4	−0.95	597.2
MO2	4–7	26.3	11.8	19.1	0.1	0.5	93.7	3.4	0.1	0.6	0.2	−0.91	448.6
MO3	7–14	27.1	12.2	20.1	0.1	0.5	94.5	3.3	0.0	0.6	0.1	−0.90	327.2
MO4	14–23	25.8	17.7	20.2	0.1	0.4	96.4	4.4	0.0	0.5	0.1	−0.94	442.4
MO5	23–38	25.1	20.1	19.8	0.1	0.4	97.3	2.7	0.0	0.4	0.0	−0.95	427.8
MO6	38–58	19.2	31.0	17.9	0.2	0.1	98.5	1.2	0.0			−0.95	374.0
MO7	58–78	22.2	33.1	16.6	0.1	0.1	99.2	0.9	0.0			−0.96	350.7
MO8	78–100	27.9	31.2	15.9	0.1	0.1	99.1	0.5	0.0			−0.98	254.8
Kaua'i 4,100 ky													
KA1	0–5	10.8	4.0	13.9	0.0	0.1	77.9	1.2	0.6	0.6	0.6	−0.99	860.3
KA2	5–11	14.4	4.0	15.6	0.0	0.1	79.7	1.2	0.2	0.3	0.3	−0.99	694.2
KA3	11–16	6.7	3.3	64.8	0.2	0.1	83.3	0.6	0.1	0.2	0.1	−1.00	398.7
KA4	16–23	22.3	7.1	35.1	0.0	0.3	94.2	1.7	0.1	0.2	0.1	−0.98	441.5
KA5	23–32	10.4	14.3	44.2	0.1	0.3	96.2	1.4	0.0	0.0	0.0	−0.88	414.1
KA6	32–43	10.3	23.8	37.8	0.2	0.1	97.2	0.7	0.0			−0.98	427.4
KA7	43–54	11.9	22.2	34.4	0.1	0.2	98.2	0.3	0.1			−0.99	417.0
KA8	54–72	13.4	26.1	34.4	0.1	0.0	98.8	0.3	0.0			−0.99	500.3
KA9	72–89	16.4	25.0	33.6	0.1	0.0	99.1	0.2	0.1			−0.99	477.9
KA10	89–100	17.2	28.5	30.2	0.1	0.0	98.1	0.2	0.0			−1.00	469.5

Note: Chemical index of alteration (CIA) is defined as molar ratios of $Al_2O_3/(Al_2O_3 + CaO^* + Na_2O + K_2O)$ by XRF, where CaO* is the amount of CaO in silicates, used to estimate the degree of chemical weathering (Nesbitt and Young, 1982). NH_4AC-K: soil K fraction extracted using NH_4AC. $\tau_{K,Nb}$: the mass transfer function of K, indexed to an immobile element (i.e. Nd, Kurtz et al., 2001).

BHVO-2 yields $\delta^{41}K$ of $-0.53 \pm 0.07‰$ (n = 7, 2S.D.). and GSP-2 yields $\delta^{41}K$ of $-0.48 \pm 0.04‰$ (n = 7, 2S.D.), consistent with literature values (Hu et al., 2018; Xu et al., 2019; Li et al., 2020a, 2020b) (Table 3). A long-term (~20 months) reproducibility (2 S.D.) for K isotope analysis obtained by measuring multiple geo-standards is $\leq 0.11‰$, and details of methodology and instrumentation are reported in Chen et al. (2019). We used a notation

Table 3
Potassium isotope composition in Hawaiian chronosequence soils.

Horizons	Depth cm	$\delta^{41}K_{Bulk}$ ‰	95% c.i. ‰	n	1 S.D. ‰	$\delta^{41}K_{NH4Ac}$ ‰	95% c.i. ‰	n	1 S.D. ‰	$\delta^{41}K_{NaBph4}$ ‰	95% c.i. ‰	n	1 S.D. ‰
Ola'a 0.3 ky													
OL1	0–3	−0.75	0.03	6	0.03	−0.30	0.06	6	0.04	−0.25	0.06	6	0.04
OL2	3–8	−0.48	0.07	7	0.07	−0.33	0.05	6	0.05				
OL3	8–13	−0.45	0.07	6	0.06	−0.38	0.07	6	0.06				
OL4	13–21	n.d.	n.d.	n.d.	n.d.	n.d.	n.d.	n.d.	n.d.				
OL5	21–27	−0.46	0.09	7	n.d.	n.d.	n.d.	n.d.	0.07				
OL6	27–36	−0.48	0.10	7	0.11	−0.42	0.06	6	0.05				
OL7	36–45	n.d.	n.d.	n.d.	n.d.	n.d.	n.d.	n.d.	n.d.				
OL8	45–64	−0.45	0.12	6	0.12	−0.46	0.07	6	0.07				
OL9	64–79	n.d.	n.d.	n.d.	n.d.	n.d.	n.d.	n.d.	n.d.				
Laupāhoehoe 20 ky													
LA1	0–5	−1.47	0.05	6	0.04	−1.13	0.06	7	0.05	−0.84	0.07	6	0.06
LA2	5–12	−1.91	0.08	7	0.09	−1.32	0.06	6	0.06				
LA3	12–20	−0.81	0.12	6	0.11	−0.47	0.07	6	0.08				
LA4	20–27	−0.51	0.04	6	0.04	n.d.	n.d.	n.d.	n.d.				
LA5	27–39	n.d.	n.d.	n.d.	n.d.	n.d.	n.d.	n.d.	n.d.				
LA6	39–52	−0.58	0.04	6	0.04	−0.19	0.06	6	0.05				
LA7	52–71	n.d.	n.d.	n.d.	n.d.	n.d.	n.d.	n.d.	n.d.				
LA8	71–94	−0.65	0.05	6	0.04	−0.14	0.08	6	0.07				
Kohala 150 ky													
KO1	0–4	−0.09	0.08	6	0.07	−0.49	0.07	6	0.05	0.06	0.08	7	0.06
KO2	4–11	−0.92	0.07	8	0.06	−0.73	0.07	7	0.06				
KO3	11–21	−1.45	0.06	6	0.06	−0.44	0.05	7	0.04				
KO4	21–30	−1.14	0.09	6	0.08	−0.47	0.07	6	0.07				
KO5	30–48	−0.70	0.04	6	0.04	n.d.	n.d.	n.d.	n.d.				
KO6	48–66	−0.52	0.09	6	0.09	−0.17	0.06	6	0.06				
KO7	66–78	n.d.	n.d.	n.d.	n.d.	n.d.	n.d.	n.d.	n.d.				
KO8	78–89	n.d.	n.d.	n.d.	n.d.	n.d.	n.d.	n.d.	n.d.				
KO9	89–98	−0.48	0.06	6	0.08	−0.19	0.07	6	0.07				
Moloka'i 1,400 ky													
MO1	0–4	−0.15	0.10	6	0.09	−0.06	0.06	6	0.05	−0.25	0.08	7	0.04
MO2	4–7	−1.05	0.05	6	0.05	−0.53	0.06	6	0.05				
MO3	7–14	−1.48	0.13	6	0.13	−0.32	0.08	6	0.07				
MO4	14–23	n.d.	n.d.	n.d.	n.d.	n.d.	n.d.	n.d.	n.d.				
MO5	23–38	−0.69	0.15	7	0.16	−0.13	0.07	7	0.07				
MO6	38–58	n.d.	n.d.	n.d.	n.d.	n.d.	n.d.	n.d.	n.d.				
MO7	58–78	−0.51	0.10	6	0.09	−0.07	0.06	6	0.05				
MO8	78–100	n.d.	n.d.	n.d.	n.d.	n.d.	n.d.	n.d.	n.d.				
Kaua'i 4,100 ky													
KA1	0–5	−0.54	0.09	7	0.04	−0.07	0.05	6	0.04	0.01	0.09	6	0.07
KA2	5–11	−1.00	0.10	7	0.10	−0.24	0.08	6	0.07				
KA3	11–16	n.d.	n.d.	n.d.	n.d.	n.d.	n.d.	n.d.	n.d.				
KA4	16–23	n.d.	n.d.	n.d.	n.d.	n.d.	n.d.	n.d.	n.d.				
KA5	23–32	−0.67	0.04	6	0.03	−0.10	0.07	7	0.07				
KA6	32–43	−0.59	0.08	6	0.07	−0.05	0.09	6	0.08				
KA7	43–54	−0.54	0.05	7	0.06	n.d.	n.d.	n.d.	n.d.				
KA8	54–72	−0.46	0.03	6	0.03	−0.02	0.07	6	0.07				
KA9	72–89	n.d.	n.d.	n.d.	n.d.	n.d.	n.d.	n.d.	n.d.				
KA10	89–109	n.d.	n.d.	n.d.	n.d.	n.d.	n.d.	n.d.	n.d.				
Pololū Lava		−0.48	0.06	7	0.08								
Hāwī Lava		−0.48	0.04	7	0.06								
USGS BHVO-2		−0.53	0.07	7	0.08								
USGS GSP-2		−0.48	0.04	7	0.05								

Note: 95% c.i. = 95% confidence interval, notates the two standard error corrected by the Student's t factor; 1S.D. = one standard deviation; n = the number of analytical cycles. $\delta^{41}K_{Bulk}$: K isotopic composition of bulk soils; $\delta^{41}K_{NH4Ac}$: K isotopic composition of soil NH_4Ac extraction; $\delta^{41}K_{NaBph4}$: K isotopic composition of soil $NaBph_4$ extraction.

$\Delta^{41}K_{x\text{-}y}$ equal to $\delta^{41}K_x$-$\delta^{41}K_y$ to express K isotope fractionation between components x and y. Confidential interval (95% c.i.) was used to reflect data statistical clarity of each sample, calculated as:

$$95\%\ \text{c.i.}\ \ (‰) = t_{n-1} \times \frac{S.D.}{\sqrt{n}} \tag{2}$$

where S.D. is the standard deviation over analytical sessions (n times) of the sample, and t_{n-1} denotes student's law factor with (n-1) degrees of freedom at a 95% confidence level. Estimated uncertainties on K isotopes were propagated based on the following equation:

$$\Delta E = \sqrt{(c_1\Delta W_1)^2 + (c_2\Delta W_2)^2 + \cdots + (c_n\Delta W_n)^2} \tag{3}$$

where ΔE is an absolute error, c is a multiplicative factor, and W is an additive function.

3.5. K XANES analysis

The K *K*-edge XANES spectra of regolith samples were acquired at the Soft X-ray Micro-Characterization beamline at Canadian Light Source (CLS). In addition to an ionization chamber and PIPS/Lytle detector, the beamline was equipped with a Si drift fluorescence detector and monochromated by diffraction from a Si(1 1 1) double-crystal monochromator, (Hu et al., 2010). After grinding, standard compounds and samples were sieved at 100-mesh (0.15 mm) and thinly spread over a double-sided K-free carbon tape adhered on a copper stick, prior to being placed in a vacuum chamber. The K *K*-edge X-ray spectra were obtained in partial fluorescence yield mode by a four-element fluorescence detector with a dwell time of 3.0 s, and the spectra of the reference standards were collected using total electron yield mode (TEY) to avoid the thickness effect. One reference (halloysite-K) was measured in fluorescence mode and conversion electron yield (CEY) mode at BL-9A at Photon Factory, KEK (Tsukuba, Japan). Sample preparation steps and analytical parameters at CLS and KEK for K *K*-edge XANES analysis were the same. The energy was calibrated using the first peak of the derivative spectra of KCl at 3.610 keV (K-edge), and no E_0 movement was noticed during data acquisition. In addition, KCl served as an internal reference and was used for energy calibration between the two beamlines. Analyses were performed in a vacuum or in a He-purged cell to suppress air-induced beam attenuation (Fig. S3), and no detectable changes in the spectra were found for repetitive scans, i.e., radiation damage should be minor.

After background removal and normalization, data were subjected to principal component analysis and the linear combination fitting to confirm possible soil K phases. Fitting was attempted using the five most possible spectra, i.e., mica-K, halloysite-K (hal-K), feldspar-K, volcanic glass (glass-K), and K in humic substances (humic-K). Information from XRD and chemical extraction was used for justification. The usage of halloysite-K as a reference is needed for this study because halloysite has been recognized as an important K host in volcanic soils (Quantin et al., 1988; Takahashi et al., 2001; Ndayiragije and Delvaux, 2004; and halloysite is enriched in studied soils (Table 1). In particular, the selectivity of halloysite to K^+ can be strengthened by coexisting Fe hydroxides (Takahashi et al., 2018), which is likely the case for this study (Table 1). Halloysite-K was prepared by mixing halloysite (200 mg, Sigma™) with 10 mM KCl solution. Glass-K represents K hosted in volcanic glass (or basaltic matrices), likely presenting in Hawaiian basalts. Humic-K is purchased from the International Humic Substances Society (IHSS). We used an R-factor to evaluate the goodness-of-fit and the significance between fits was gained from a Hamilton test ($p < 0.05$; Calvin, 2013) with a number of independent data points calculated by re-normalization to a sum of 100%. When adding more K references, if an R-factor was not significantly better based on a Hamilton test, fits with fewer references were preferred to preclude overfitting. If two fits with the same number of references are comparable, results are averaged (Table 4). Data processing was performed using the software Athena (Ravel and Newville, 2005).

3.6. Source quantification

Relative contributions of major K sources (mineral aerosols, marine aerosols, and basaltic substrate) to chronosequence soils were quantified, as have been investigated for Li, Mg, and U in the same sites (Pett-Ridge et al., 2007; Ryu et al., 2014; Ryu et al., 2020).

The K inputs from mineral aerosols are calculated assuming that the element composition of Asian dust accumulating in Hawaiian soils has remained relatively homogeneous over the past 4,100 ky (Kyte et al., 1993):

$$K_{Dust} = C^K_{Dust} \cdot F_{Dust} \cdot t \tag{4}$$

where C^K_{Dust} is the average K concentration in the upper continental crust (UCC; $[K_2O] = 2.8$ wt%; Rudnick and Gao, 2013), F_{Dust} denotes the average long-term dust accretion rate in Hawai'i (30 mg/(cm^2·ky) for the younger sites < 20 ky and 125 mg/(cm^2·ky) for the older sites ≥ 20 ky; Kurtz et al., 2001), and t is the age of the lava substrate (0.3–4,100 ky).

Next, total K inputs from marine aerosols were estimated as follows:

$$K_{Marine} = C^K_{Marine} \cdot MAP \cdot t \tag{5}$$

where K_{Marine} denotes the K concentrations in local rain measured at three sites in the islands (5.3 μmol/L at Thurston, Hawai'i, and 0.7 μmol/L, Kaua'i, Carrillo et al., 2002; 1.3 μmol/L in Hawai'i of similar elevations as chronosequence soil sites, Eriksson, 1957). The MAP value is 2500 mm/yr, and t is the age of lava substrate (0.3–4,100 ky). It is necessary to note that [K] in local rainwater from 1993 to 2000 varies about two orders of magnitudes, which may cause bias in the estimation of K_{Marine}. Therefore, we consider both the high (5.3 μmol/L) and the low values (0.7 μmol/L) based on Carrillo et al. (2002).

Similarly, K inputs sourced from the basaltic substrate can be calculated as follows:

Table 4
Potassium XANES-LCF speciation in Hawaiian chronosequence soils.

Horizons	Depth cm	Hal-K %	Mica-K %	Glass-K %	Feldspar-K %	Humic-K %	R
Ola'a 0.3 ky							
OL1	0–3	0 (0)	0 (0)	19 (2)	29 (0)	53 (2)	0.008
OL2	3–8	0 (0)	0 (0)	67 (1)	20 (1)	13 (2)	0.003
OL3	8–13	0 (0)	0 (0)	71 (1)	6 (1)	0 (0)	0.001
OL4	13–21	23 (1)	0 (0)	76 (1)	5 (1)	0 (0)	0.001
OL5	21–27	18 (1)	0 (0)	60 (1)	40 (1)	0 (0)	0.007
OL6	27–36	0 (0)	0 (0)	57 (2)	43 (1)	0 (0)	0.011
OL7	36–45	0 (0)	0 (0)	61 (1)	39 (1)	0 (0)	0.005
OL8	45–64	0 (0)	0 (0)	57 (2)	43 (1)	0 (0)	0.007
OL9	64–79	0 (0)	0 (0)	46 (2)	54 (1)	0 (0)	0.007
Laupāhoehoe 20 ky							
LA1	0–5	10 (2)	8 (1)	0 (0)	0 (0)	82 (1)	0.003
LA2	5–12	38 (3)	30 (2)	0 (0)	0 (0)	32 (2)	0.009
LA3	12–20	0 (0)	83 (2)	0 (0)	0 (0)	17 (2)	0.013
LA4	20–27	0 (0)	91 (2)	0 (0)	0 (0)	0 (0)	0.012
LA5	27–39	9 (2)	100 (0)	0 (0)	0 (0)	0 (0)	0.009
LA6	39–71	0 (0)	100 (0)	0 (0)	0 (0)	0 (0)	0.012
LA8	71–94	0 (0)	100 (0)	0 (0)	0 (0)	0 (0)	0.038
Kohala 150 ky							
KO1	0–4	0 (0)	41 (2)	0 (0)	0 (0)	59 (2)	0.015
KO2	4–11	0 (0)	62 (2)	0 (0)	0 (0)	38 (2)	0.012
KO3	11–21	30 (6)	70 (6)	0 (0)	0 (0)	0 (0)	0.034
KO4	21–30	29 (4)	71 (4)	0 (0)	0 (0)	0 (0)	0.032
KO5	30–48	16 (2)	84 (2)	0 (0)	0 (0)	0 (0)	0.010
KO6	48–66	10 (3)	90 (2)	0 (0)	0 (0)	0 (0)	0.016
KO7	66–78	7 (1)	93 (2)	0 (0)	0 (0)	0 (0)	0.027
KO8	78–89	0 (0)	100 (0)	0 (0)	0 (0)	0 (0)	0.011
KO9	89–98	0 (0)	100 (0)	0 (0)	0 (0)	0 (0)	0.013
Moloka'i 1,400 ky							
MO1	0–4	16 (2)	48 (1)	0 (0)	0 (0)	38 (1)	0.003
MO2	4–7	0 (0)	71 (2)	0 (0)	0 (0)	29 (2)	0.012
MO3	7–14	0 (0)	80 (3)	0 (0)	0 (0)	20 (3)	0.009
MO4	14–23	0 (0)	100 (0)	0 (0)	0 (0)	0 (0)	0.016
MO5	23–38	0 (0)	100 (0)	0 (0)	0 (0)	0 (0)	0.013
MO6	38–58	0 (0)	100 (0)	0 (0)	0 (0)	0 (0)	0.009
MO7	58–78	0 (0)	100 (0)	0 (0)	0 (0)	0 (0)	0.016
MO8	78–100	0 (0)	100 (0)	0 (0)	0 (0)	0 (0)	0.017
Kaua'i 4,100 ky							
KA1	0–7	11 (1)	16 (1)	0 (0)	0 (0)	73 (1)	0.003
KA2	7–11	0 (0)	59 (4)	0 (0)	0 (0)	41 (4)	0.019
KA3	11–16	0 (0)	76 (2)	0 (0)	0 (0)	24 (3)	0.012
KA4	16–23	0 (0)	100 (0)	0 (0)	0 (0)	0 (0)	0.027
KA5	23–32	0 (0)	100 (0)	0 (0)	0 (0)	0 (0)	0.010
KA6	32–43	0 (0)	100 (0)	0 (0)	0 (0)	0 (0)	0.010
KA7	43–54	0 (0)	100 (0)	0 (0)	0 (0)	0 (0)	0.021
KA8	54–72	0 (0)	100 (0)	0 (0)	0 (0)	0 (0)	0.020
KA9	72–89	0 (0)	100 (0)	0 (0)	0 (0)	0 (0)	0.031

Note: The R factor is the goodness-of-fit parameter of XANES-LCF reported by Athena ($R = \Sigma(\text{data fit})^2/\Sigma(\text{data})^2$; Ravel and Newville, 2005). The standard errors in the parentheses are for the LCF analysis provided by Athena software although the actual uncertainties for the overall XANES-LCF analysis could be lower.

$$K_{Basalt} = C^{K}_{Basalt} \cdot z_t \cdot S_c \cdot \rho_{Basalt} \quad (6)$$

where K_{Basalt} is the K concentration in basalts (3.3 g/kg for 0.3, 1,400 and 4,100 ky, 6.6 g/kg for 20 ky, and 14.9 g/kg for the 150 ky site; Ziegler et al., 2005), z_t denotes the total regolith thickness (cm), S_c is the collapse factor, and ρ_{Basalt} is averaged basalt density (1.25 g/cm^3; Chadwick et al., 2003).

A combination of Eqs. (4)–(6) allows us to calculate total K addition from allochthonous and basaltic sources. The overall regolith thickness directly depends on their ages (Pett-Ridge et al., 2007), but the thickness is difficult to determine due to local variability linked to void spaces and hydrological permeability (Goodfellow et al., 2014).

Table 5
Results of K mass-balance calculation in Hawaiian chronosequence soils.

Age	Collapse factor[2]	$K_{Present}$[3]	K_{Total}[4]				K_{Loss}[5,a]	K_{Loss}[5.b]
			K_{Basalt}	K_{Dust}	K_{Marine}[a]	K_{Marine}[b]		
ky	Sc	mg/cm^2	mg/cm^2	mg/cm^2	mg/cm^2	mg/cm^2	mg/cm^2	mg/cm^2
0.3	0.7	288.31	373.4	0.21	2.31	0	85.3	85.3
20	0.8	53.78	663.83	13.94	624.16	1.06	624.19	625.05
150	1.5	147.02	2800.5	435.64	3090.59	7.738	3090.58	3096.858
1,400	2	102.24	829.75	4065.95	4807.12	72.345	4807.11	4865.805
4,100	4.5	47.29	1866.94	11907.4	13767.1	211.894	13767.06	13938.97

[1]Values represent mass-weighted averages of soil horizons to 1-m depth.
[2] Collapse factor is the ratio of the present Nb inventory in the soil (Nb_{Soil}) to the total Nb coming from the parent basalt (Nb_{Basalt}).
[3] Depth-integrated K based on measured K concentration and density.
[4] Basalt [K_2O] and [Nb] data are from Ziegler et al. (2005).
[5] $K_{Loss} = K_{Total} - K_{Present}$.
[a] Values calculated using 0.7 μmol/L K for rainwater estimation.
[b] Values calculated using 5.3 μmol/L K for rainwater estimation.

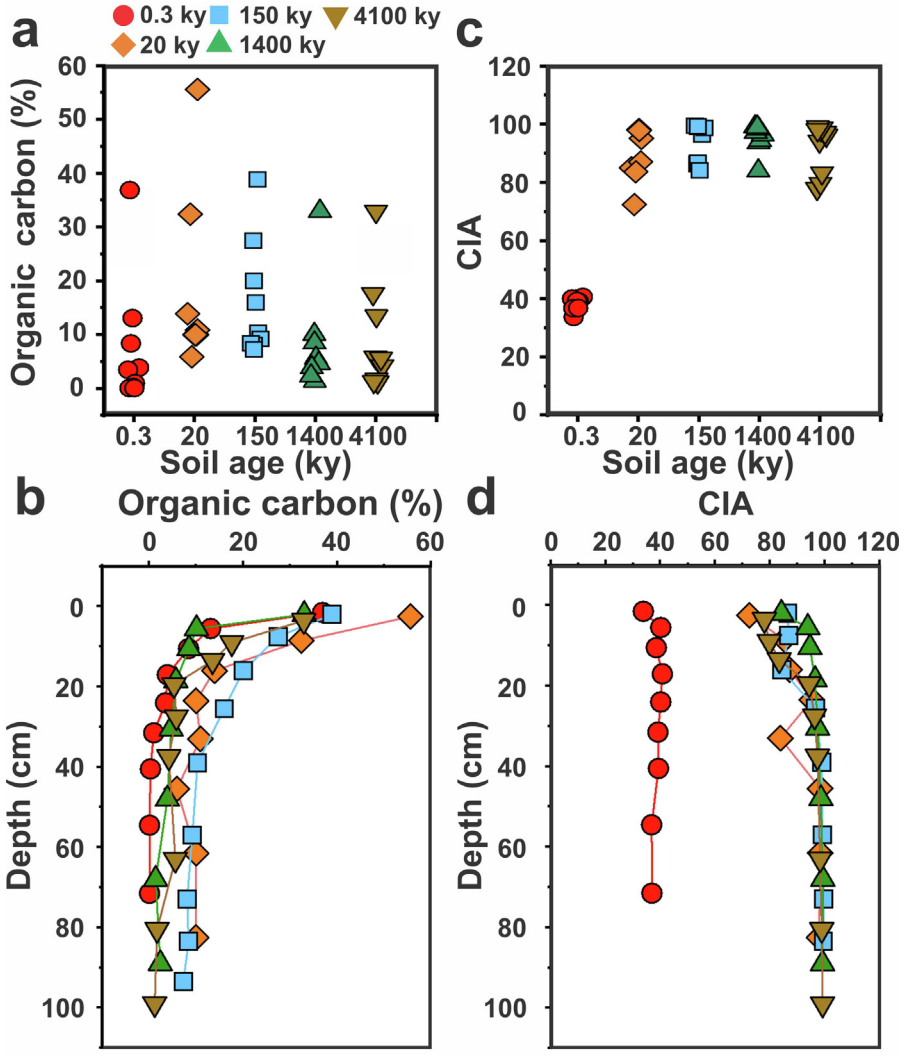

Fig. 3. The development of (a–b) organic carbon, and (c–d) chemical weathering index (CIA) of soils along the chronosequence. Data points in the upper panels are arrayed in the sequence of ages from 0.3 to 4,100 ky. Data points in the deeper panels are shown in in-depth profiles. Data in the plot are summarized in Table 2.

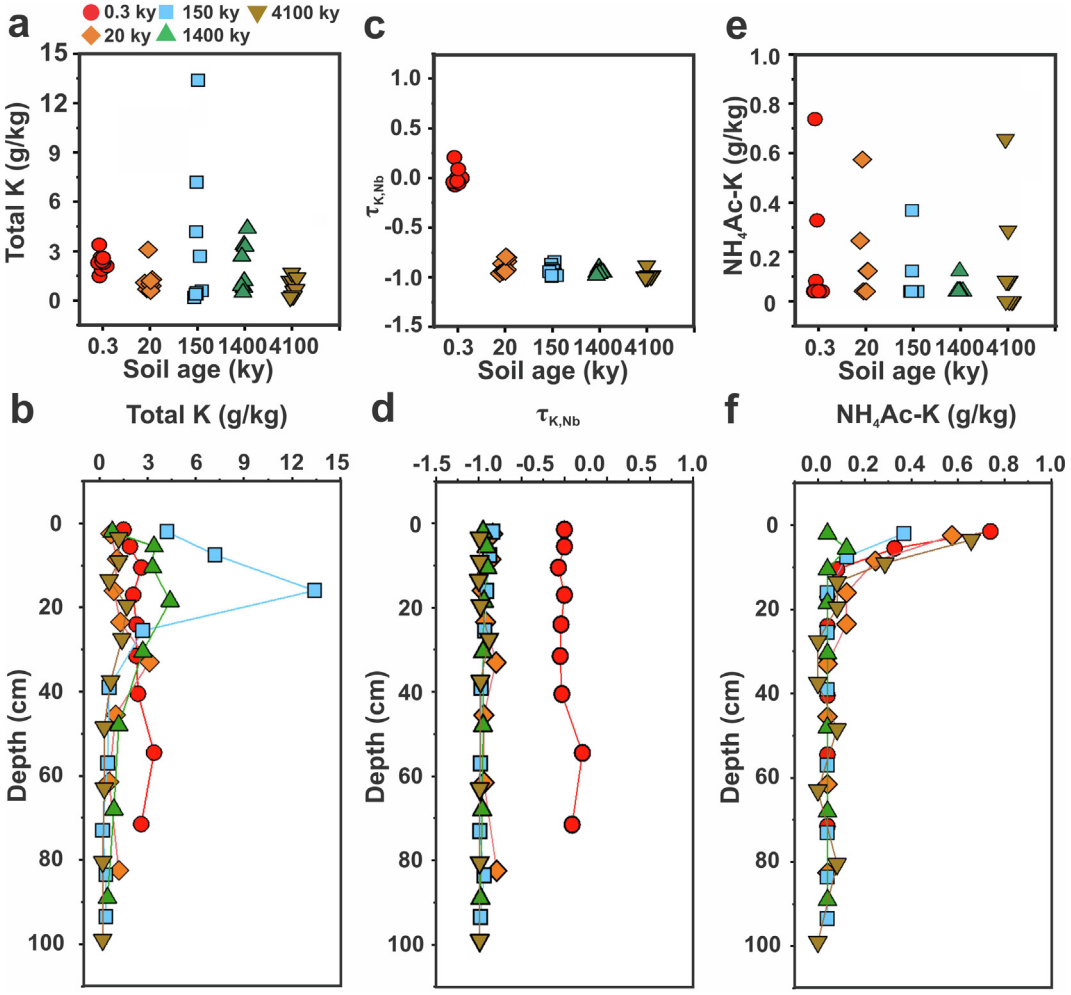

Fig. 4. The patterns of (a–b) K concentration [K], (c–d) the mass transfer coefficient of K (indexed to less mobile Nb, $\tau_{K,Nb}$, Kurtz et al., 2000) and (e–f) NH_4Ac-extracted K of soils along the chronosequence. Data points in the upper panels are arrayed in the sequence of ages from 0.3 to 4,100 ky. Data points in the panels (b–f) are shown in in-depth profiles. Data in the plot are summarized in Table 2.

We thus calculated values representing soil horizons to 1-m depth, which is a common approach (Ryu et al., 2020). Further, we can compare total K inputs corresponding to the regolith residence time with the present K in the regolith $K_{Present}$ (i.e., depth-integrated K mass per unit area). Hence, the difference between two parameters allows for an estimate of total K loss from the site:

$$K_{Present} = \sum_h (C_h^K \cdot z_h \cdot \rho_h \quad (7)$$

$$F_{Loss}(\%) = \left[K_{Present}/(^K_{Basalt} + K_{Marine} + K_{Dust}\right) - 1) \times 100 \quad (8)$$

where C_h^K is the K concentration in each soil horizon, and results are provided in Table 5.

4. RESULTS

4.1. Soil organic carbon and CIA

Soil organic carbon content increases from 0.3 ky (0.1–36.9%) to 20 ky (5.9–55.6%) soils and decreases from 20 to 150 ky (7.3–38.9%), 1,400 ky (1.4–33.0%) and 4,100 ky (1.2–32.9%) soils. In all sites, we find a vertical enrichment of soil organic carbon, with the degree of accumulation most significant at <20 cm and reaching the maximum at the top. Age-dependent soil organic carbon content (Fig. 3a and b) follows a similar pattern as the forest productivity in this chronosequence (Fig. S1, Torn et al., 1997).

The chemical index of alteration (CIA) has been estimated using the XRF-based oxide composition, indicating intense weathering (CIA ~ 90) at all sites except for the youngest site of 0.3 ky (Fig. 3c). The CIA values remain nearly constant at depths >20 cm but are slightly lower in the surface horizons which have been mixed with mineral aerosol derived from continental sources (Kurtz et al., 2001) (Fig. 3c and d).

4.2. Soil K concentration

Soil K concentrations ([K]) and mass transfer coefficient ($\tau_{K,Nb}$) vary with the substrate age and depth and fall in ranges of 0.2 to 13.4 g/kg and −1.00 to 0.21, respectively (Table 2 and Fig. 4). At the 0.3 ky site, [K] slightly increases

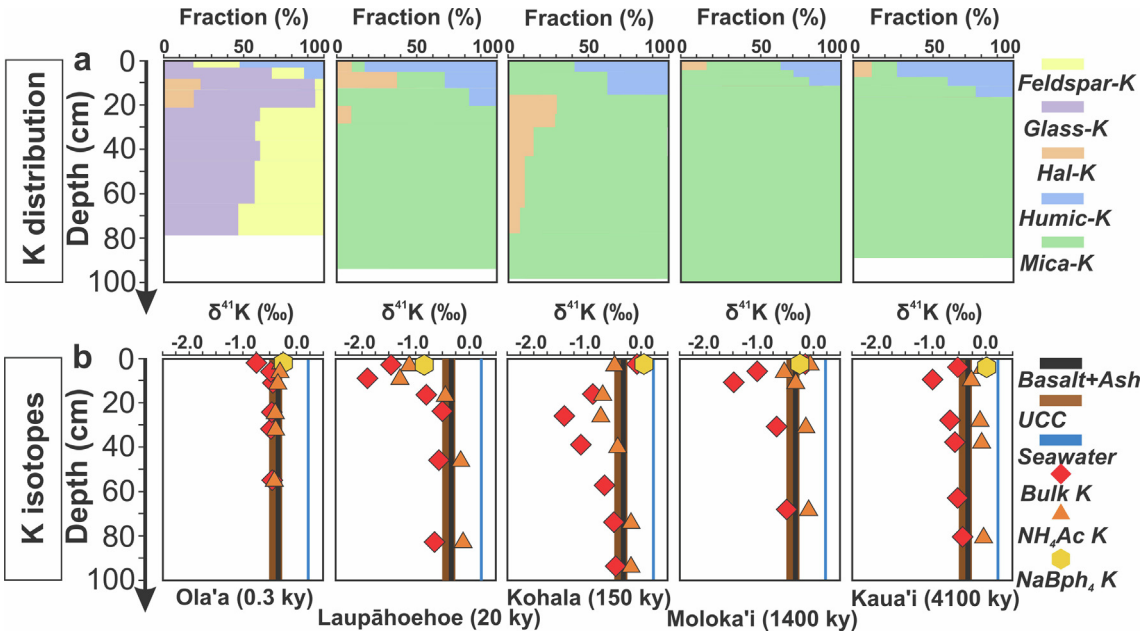

Fig. 5. Vertical profiles of (a) the distribution of K phases (K *K*-edge XANES-LCF, Table 4), and (b) soil K isotope composition (Table 3). In plot (b), $\delta^{41}K$ of basaltic materials (i.e., basalts and ashes), the upper continental crust (UCC, Huang et al., 2020), and seawater (Hille et al., 2019; Wang et al., 2020) are symbolized using black, brown, and blue bars, respectively. NH_4Ac-K and $NaBph_4$-K fractions indicate NH_4Ac-extracted (exchangeable) and $NaBph_4$-extracted (interlayered) K. Original spectra and references for XANES-LCF are provided in Fig. S3. Symbol sizes are larger or about the same as errors. Numerical XANES data are provided in the SI. (For interpretation of the references to colour in this figure legend, the reader is referred to the web version of this article.)

downwards (1.5–3.4 g/kg). At the 20 ky site, K is relatively depleted across the profile (0.6–1.2 g/kg) except for the peak enrichment (3.1 g/kg) at the 27–29 cm interval. At the 150 ky site, [K] is relatively high for the upper horizon (<20 cm, 2.7–13.4 g/kg) with the peak enrichment of 13.4 g/kg at the 11–21 cm interval and decreases to 0.2–0.6 g/kg for the deeper horizons. At the 1,400 ky site, [K] is low at the surface (0.8 g/kg) and enriches at the 4–38 cm depth (2.7–4.4 g/kg) with a downward decrease (0.5–1.2 g/kg). At the 4,100 ky site, [K] is relatively high at the 0–32 cm interval (0.6–1.7 g/kg) and low at the deeper units (0.2–0.7 g/kg). The $\tau_{K,Nb}$ value for the youngest soil varies within a narrow range of −0.07 to 0.21 (i.e., negligible mass change in K relative to the basaltic substrate). In the older soil sites (≥20 ky), $\tau_{K,Nb}$ value approaches ~−1.0 (Fig. 4c and d). Overall, most K released from basalt leaching is lost in the soils older than 0.3 ky and a small amount of remaining K is either held within soil organic matter or clay minerals (e.g., adsorption to their negatively charged surfaces).

The trends of NH_4Ac-K and organic-K are vertically similar, and the good correspondence between NH_4Ac-K and organic-K implies that organic-K is exchangeable (Fig. S4a). The NH_4Ac-K (exchangeable K) is enriched in the upper horizons (<20 cm), and NH_4Ac-K declines to ~0 in the deeper horizons (Fig. 4e and f). The NH_4Ac-K concentration falling in ranges of 0.0–0.7 g/kg (0.3 ky), 0.0–0.6 g/kg (20 ky), 0.0–0.4 g/kg (150 ky), 0.0–0.4 g/kg (1,400 ky) and 0.1–0.6 g/kg (4,100 ky). The organic-K extracted by H_2O_2 (K in soil organic matter) is enriched in the topsoils (0.6 g/kg, 0.3 ky; 0.6 g/kg, 20 ky; 1.0 g/kg, 150 ky; 0.4 g/kg, 1,400 ky; 0.6 g/kg, 4,100 ky) and downward decrease (0.1–0.4 g/kg, 0.3 ky; 0.0–0.2 g/kg, 20 ky; 0.0–0.5 g/kg, 150 ky; 0.0–0.2 g/kg, 1,400 ky; 0–0.3 g/kg, 4,100 ky). The concentration of NH_4Ox-K (a sum of organic-K and SRO-K) fall in the ranges of 0.7–1.3 g/kg (0.3 ky), 0.0–0.6 g/kg (20 ky), 0.1–1.3 g/kg (150 ky), 0.4–0.6 g/kg (1,400 ky) and 0.0–0.6 g/kg (4,100 ky) (Table 2).

4.3. Soil K distribution

We classify soil K into five most likely phases, including hal-K (K linked with halloysite), feldspar-K (K in feldspars), glass-K (K in basaltic glass), humic-K (K in humic substances), and mica-K (dust-derived K in mica/illite) (Table 4). The glass-K and feldspar-K are the dominant phases in 0.3 ky site, making up 19–76% and 5–54% total K, respectively. The hal-K occurs in all sites but can only be identified at some depth intervals. The humic-K makes up 0 to 82% of K and occurs in 0.3–4,100 ky sites, particularly in the topsoils. The mica-K phase is negligible in the 0.3 ky site but makes up most of K in other sites (8–100%, 20 ky; 41–100%, 150 ky; 48–100%, 1,400 ky; 16–100%, 4,100 ky). The mica-K fraction increases from the upper units (<20 cm) to the deeper units (Fig. 5a).

4.4. Soil K isotope composition

Bulk soil $\delta^{41}K$ values range from $-0.75 \pm 0.03‰$ to $-0.45 \pm 0.07‰$ (0.3 ky), $-1.47 \pm 0.05‰$ to $-0.51 \pm 0.04‰$ (20 ky), $-1.45 \pm 0.06‰$ to $-0.09 \pm 0.08‰$ (150 ky), $-1.48 \pm 0.13‰$ to $-0.15 \pm 0.10‰$ (1,400 ky), and $-1.00 \pm 0.10‰$ to $-0.46 \pm 0.03‰$ (4,100 ky) and vary with

depth (Table 3 and Fig. 5b). The 0.3 ky site shows little variation in $\delta^{41}K$ (about −0.45‰), except for the topmost soil horizon (−0.75 ± 0.03‰). In the 20 ky site, $\delta^{41}K$ in the upper horizon displays overall bulk soil $\delta^{41}K$ lower than the basaltic substrate with a minimum (−1.91 ± 0.08‰) occurring at 5–12 cm depth. In the older sites, a maximum $\delta^{41}K$ appears at the surface (−0.09 ± 0.08‰, 150 ky; −0.15 ± 0.10‰, 1,400 ky; −0.54 ± 0.09‰, 4,100 ky), close to $\delta^{41}K_{Basalt}$ or $\delta^{41}K_{Seawater}$ (~0.14‰, Hille et al., 2019; Wang et al., 2020). At the subsurface (10–20 cm), bulk soil $\delta^{41}K$ values are lower than $\delta^{41}K_{Basalt}$, displaying the minimum of −1.45 ± 0.06‰ (11–21 cm, 150 ky), −1.48 ± 0.13‰ (7–14 cm, 1,400 ky), and −1.00 ± 0.10‰ (7–11 cm, 4,100 ky). The deeper horizons (>30 cm) have $\delta^{41}K$ comparable to $\delta^{41}K_{Basalt}$. The magnitude of bulk soil $\delta^{41}K$ variation follows an order: 0.3 < 4,100 < 1,400 ≈ 150 ≈ 20 ky.

Soil $\delta^{41}K_{NH4Ac}$ values range from −0.46 ± 0.07‰ to −0.30 ± 0.06‰ (0.3 ky), −1.32 ± 0.06‰ to −0.14 ± 0.08‰ (20ky), −0.73 ± 0.07‰ to −0.17 ± 0.06‰ (150ky), −0.53 ± 0.06‰ to −0.05 ± 0.05‰ (1,400 ky), and −0.24 ± 0.08‰ to −0.02 ± 0.07‰ (4,100 ky) and vary with depth (Table 3 and Fig. 5b). In the 0.3 ky soil site, there is a downward decreasing pattern of $\delta^{41}K_{NH4Ac}$, approaching to $\delta^{41}K_{Basalt}$. In sites older than 0.3 ky, the maximum $\delta^{41}K_{NH4Ac}$ appears at the surface with dramatic decreases in $\delta^{41}K_{NH4Ac}$ at the subsurface ~10–20 cm, more positive than the corresponding bulk soil $\delta^{41}K$. The minimum $\delta^{41}K_{NH4Ac}$ along each profile occurs at the subsurface layer (−1.32 ± 0.06‰, 20ky; −0.73 ± 0.07‰, 150 ky; −0.53 ± 0.06‰, 1,400 ky; −0.24 ± 0.08‰, 4,100 ky). In the deeper layer, there is an increasing pattern of $\delta^{41}K_{NH4Ac}$ value downwards that can be more positive than $\delta^{41}K_{Basalt}$ but more negative than $\delta^{41}K_{Seawater}$. The degree of isotopic variation in $\delta^{41}K_{NH4Ac}$ (exchangeable K) follows an order: 0.3 < 4,100 < 1,400 ≈ 150 ≈ 20 ky.

The NaBph4 extracts have been measured on surface soils only. Soil $\delta^{41}K_{NaBph4}$ values are −0.25 ± 0.06‰ (0.3 ky), −0.84 ± 0.07‰ (20ky), 0.06 ± 0.08‰ (150ky), −0.25 ± 0.08‰ (1,400 ky), and 0.01 ± 0.09‰ (4,100 ky), increasing as the substrate ages.

4.5. K inputs estimation

By mass-based accumulative calculation, the amounts of K supplied by basalt weathering are 373.4 (0.3 ky), 663.83 (20 ky), 2800.50 (150 ky), 829.75 (1,400 ky), and 1866.94 (4,100 ky) mg/cm^2. The amounts of K delivered by mineral aerosols are 0.21 (0.3 ky), 13.94 (20 ky), 435.64 (150 ky), 4065.95 (1,400 ky) and 111907.4 (4,100 ky) mg/cm^2. The amounts of K delivered by marine aerosols are 0.0 (0.3 ky), 0.14 (20 ky), 1.02 (150 ky), 9.56 (1,400 ky) and 27.99 (4,100 ky) mg/cm^2 (using average rainwater K of 0.7 μmol/L). Alternatively, the amounts of K delivered by marine aerosols were 0.0 (0.3 ky), 1.06 (20 ky), 7.74 (150 ky), 72.35 (1,400 ky) and 211.89 (4,100 ky) mg/cm^2 (assuming average rainwater K of 5.3 μmol/L) (Table 5). The data reveal that K from basalts provided ~99% (0.3 ky), ~98% (20 ky) and ~85% (150 ky) of K_{Total} to soil sites, and K delivered by mineral aerosols becomes dominant in 1,400 (~82%) and 4,100 ky (~85%) sites. The K inputs of marine aerosols are minor (<2%). Total loss of K increases from 2.31 to 13767.05 mg/cm^2 and K loss level ($K_{Present}$ relative to K_{Total}) reaches ~−100%, as the substrate ages. The estimation implies K inputs over time rather than contributions to present the soil K pool.

5. DISCUSSION

We first evaluate soil K allocation based on spectral interpretation of K *K*-edge XANES combined with results from chemical extraction and mineralogy. Next, we investigate how the dominant phases that contain K contribute to variations in soil $\delta^{41}K$. We illustrate the causes of K isotope variations in vertical profiles as well as with increasing substrate age. Moreover, we discuss similarities and differences between K isotopes and other isotopes along the chronosequence. Finally, we provide potential implications for tracing chemical weathering and biogeochemical cycles of K in terrestrial environments.

5.1. The allocation of K in studied soils

The phase partitioning of K in soils can be estimated by the linear combination fitting (LCF) of XANES using five reference spectra, which offers insights into the allocation of K along the chronosequence (Table 4). We note that XANES-LCF only provides mathematical estimation without geological meaning. The result of XANES-LCF (Table 4) can provide a first-order estimate of K phase distribution in studied soils but the insight gained from LCF may be limited by the reference spectra available. Inclusion of additional reference spectra may enable greater insights into species present. For example, extracted NH_4Ox-K is more than NH_4Ac-K and H_2O_2-K in soil samples (Fig. S4), which cannot be explained by the XANES-LCF data. It is possible that some K is associated with SRO materials that may be extracted by NH_4Ox (e.g., K trapped within SRO aggregates containing allophane, Chorover et al. 2004). However, this type of SRO-K phase remains elusive and is not considered in the fitting.

In the youngest soil (0.3 ky), K predominantly presents in feldspar-K and glass-K. In the older soils, progressively greater amounts of K are associated with organic matter and mica (Fig. 5a). The occurrence of feldspar-K in the youngest soil site (0.3 ky) is expected because this site experienced weak weathering as evidenced by CIA of ~35–40 (close to the fresh basalt, Nesbitt and Young, 1982), $\tau_{K, Nb}$ of ~0 (negligible K loss/gain), and the dominance of feldspars (and other primary components) based on XRD data (Fig. 2a and S2). The glass-K fraction is also enriched (19 to 76%) in the 0.3 ky site. We suggest that the K XANES spectrum without clear peaks of glass-K probably reflects the K atoms situating in poorly crystalline, disordered sites (Fig. S3). All sites contain kaolin minerals (primarily halloysite) and XANES identifies some K (<40%) are associated with halloysite, in particular for 20–150 ky sites (Fig. S2 and Table 1). Although we do not have a resolution to know if K is adsorbed as outer-sphere or inner-sphere complexes at the interlayers of halloysite, Takahashi

et al. (2018) experimentally confirmed the dehydration of K^+ before interlayer occupation.

Humic-K is enriched in the topsoils of all studied sites (Table 4), and the quantification of humic-K by XANES corresponds well with chemically extracted organic-K (Fig. S4c). The presence of humic-K probably reflects K derived from plant decay. Soil organic matter mainly derives from litterfall, and biological exudates potentially promote the enrichment of humic-K in soils. In the older sites, the decrease in the forest cover (Fig. S1) dampens plant imprints on soil K, and the proportion of humic-K in 150 to 4,100 ky soils is less than that of the 20 ky site. We infer that organic-bound K may be replaced by competitive ions such as Al^{3+} (Chorover et al., 2004) during soil development, thus reducing the humic-K fraction in the older sites.

We suggest that mica-K identified in studied soils is of an exogenous origin rather than an authigenic origin. Marked mineral aerosol inputs to Hawaiian soils have been reported in the literature, and quartz and illite/mica in the chronosequence soils are derived from mineral aerosols (Kurtz et al., 2001). Soil K concentration at ~20 cm in 150 ky site is about 4–5 times higher than those of other sites, corresponding to the enrichment of mica/illite (Fig. 2a) and larger tau values compared to other sites except for the 0.3 ky site (Fig. 4f). However, such a pattern is not reflected on XANES (Fig. 5a), which only demonstrates K phase partitioning rather than the enrichment level of K. In addition, XANES-based mica-K is more abundant in the deeper layers (up to 100%) even though XRD-based mica/illite is more enriched in the upper layers (Figs. 2a and 5a). Although there is less mica/illite in the deeper soils, they may go a long way in determining the whole soil K budget due to long-term leaching of basalt K in soils older than 0.3 ky and the K-rich nature of mica/illite.

Radiogenic Nd and Sr isotopes have long been used as reliable tracers of atmospherically sourced contributions to Hawaiian soils (e.g., Stewart et al., 2001; Kurtz et al. 2001). For example, Arendt et al. (2015) used Nd-Sr mixing models based on data in Kurtz et al. (2001) and quantified the contribution of basalts, mineral, and marine aerosols in soils (Fig. 2b). The Nd-Sr model in Arendt et al. (2015) showed the convergence back to the "bedrock" signals at the oldest soil site (4,100 ky) (Fig. 2b), as opposed to the complete depletion of primary K based on XRD and XANES (Figs. S2 and S3). It is shown that primary phases were fully consumed before 20 ky (Kennedy et al., 1998). Using Eqs. (4)–(8), we could calculate the contribution of each K source to the soil K budget and K loss (Table 5), showing nearly one magnitude higher K_{Dust} than K_{Basalt} in the 4,100 ky site, distinct from Arendt et al. (2015) models. To explain the discrepancy between Nd-Sr models with XANES and mass-balance results, we infer that Nd and Sr are available in high quantities in lavas relative to mineral aerosols, and K is enriched in mineral aerosols than basalts. Model estimation using $^{87}Sr/^{86}Sr$ and εNd likely offers a

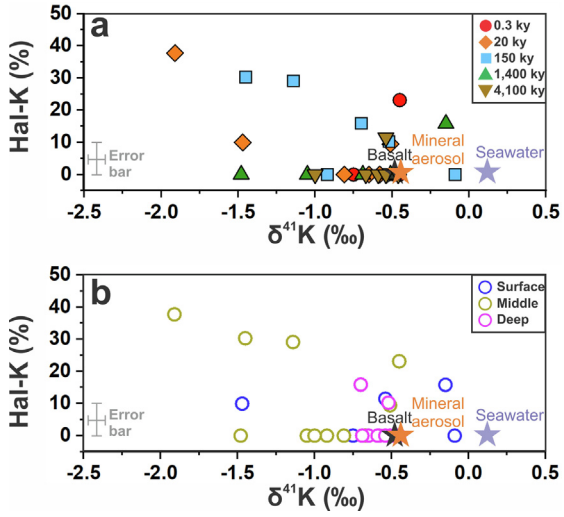

Fig. 6. The comparison between soil K isotope compositions and hal-K fraction (i.e., K hosted by halloysite based on XANES-LCF). In plot (a), soil sites with different substrate ages are marked. In plot (b), samples from different depth intervals are marked. The black, orange and purple stars represent parent basalts, mineral aerosols ($\delta^{41}K_{UCC}$ in Huang et al., 2020), and seawater ($\delta^{41}K_{SEA}$, Hille et al., 2019; Wang et al., 2020), respectively. The XANES-LCF generally has a 10% systematic error (Singh and Grafe, 2010) and the long-term 2 S.D. uncertainty of K isotope analysis is 0.11‰ (Chen et al., 2019). (For interpretation of the references to colour in this figure legend, the reader is referred to the web version of this article.)

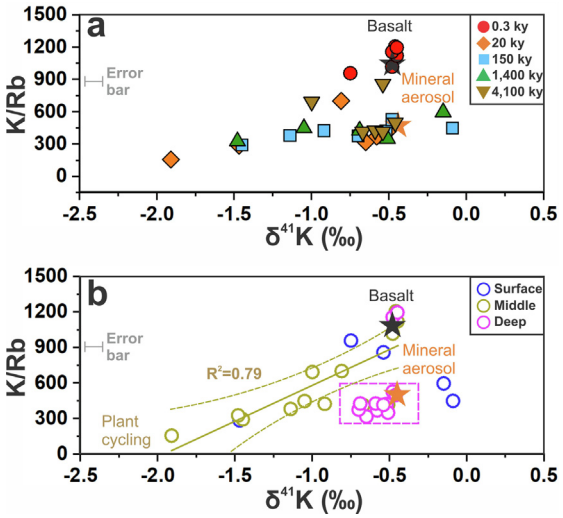

Fig. 7. The comparison between soil K isotope compositions and K/Rb ratio. In plot (a), soil sites with different substrate ages are marked. In plot (b), soil samples from different depth intervals are distinguished. The black and orange stars denote the values of basalts and mineral aerosols ($\delta^{41}K_{UCC}$ in Huang et al., 2020, and K/Rb_{UCC} in Rudnick and Gao, 2013), respectively. In plot (b), the linear fitting is shown with 95% confidence bands. The purple square shows similarities between soils of the deep horizons and mineral aerosols. The XANES-LCF generally has a 10% systematic error (Singh and Grafe, 2010) and the long-term 2 S.D. uncertainty of K isotope analysis is 0.11‰ (Chen et al., 2019). (For interpretation of the references to colour in this figure legend, the reader is referred to the web version of this article.)

direct measure of Sr-Nd sources, but cannot precisely clarify the allocation of K.

5.2. Controls on soil $\delta^{41}K$ variability

5.2.1. General evaluation

Based on Section 5.1, we summarize three major controls on soil K budgets that may lead to K isotope variations, including (i) basalt weathering and clay formation, (ii) plant cycling, and (iii) source mixing, which has been extensively discussed in previous Hawaiian soil research. Herein, we can use several reliable proxies to determine the control of Earth surface processes on soil K isotope composition. First, the impact of basalt weathering and clay formation on bulk soil $\delta^{41}K$ can be estimated by the proportion of clay-K fraction (without dust-derived mica-K) from XANES-LCF (Table 4). In most cases, clay formation with preferential ^{39}K partitioning into secondary residues plays a critical role in terrestrial settings, causing the K isotope fractionation of ~0.5‰ (e.g., Li et al., 2019; Chen et al., 2020; Teng et al., 2020; Wang et al., 2021; Li et al., 2021c). Using the hal-K fraction should be better than a common clay formation proxy K_2O/Al_2O_3 (Huang et al., 2020) for this study since many clay minerals do not contain significant amounts of K. We exclude mica-K as a potential K source of authigenic clays is because mica in Hawaiian soils is only derived from the Asian dust transported over long distances (Kurtz et al., 2001). The comparison between bulk soil $\delta^{41}K$ and hal-K is provided in Fig. 6a. Soils with high hal-K (~25–40%) display much lower $\delta^{41}K$ than that of the basalt by up to ~1.5‰. Chemical weathering (and soil formation) is unlikely the only cause for such a large isotopic fractionation and additional controlling factors are provided below.

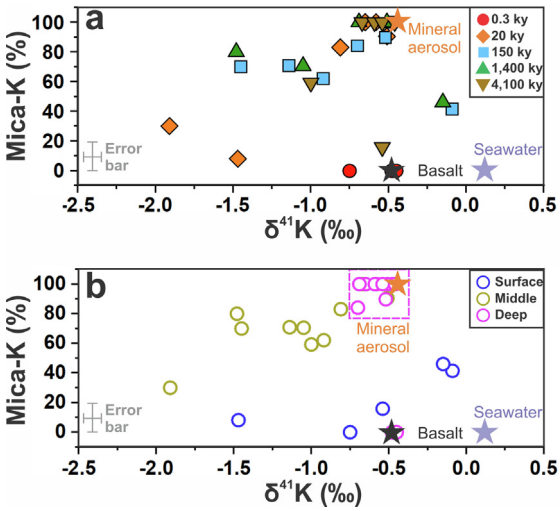

Fig. 8. The comparison between soil K isotope compositions and XANES-based mica-K fraction. In plot (a), soil sites with different substrate ages are marked. In plot (b), soil samples from three depth intervals are distinguished. The black, orange and purple stars represent the data of basalts, mineral aerosols ($\delta^{41}K_{UCC}$ provided in Huang et al., 2020), and seawater ($\delta^{41}K_{SEA} \sim 0.14‰$, Hille et al., 2019; Wang et al., 2020), respectively. In plot (b), the purple square highlights the K phase (mica-K rich) and K isotope compositions of soil samples at the deep horizon close to those of mineral aerosols. The XANES-LCF generally has a 10% systematic error (Singh and Grafe, 2010) and the long-term 2 S.D. uncertainty of K isotope analysis is 0.11‰ (Chen et al., 2019). (For interpretation of the references to colour in this figure legend, the reader is referred to the web version of this article.)

The comparison between soil $\delta^{41}K$ and K/Rb is provided in Fig. 7a, indicating critical plant imprints on soil budgets. The role of biogeochemical cycling in modifying bulk soil $\delta^{41}K$ can be estimated from the change in soil K/Rb ratio because of similar physicochemical properties but distinct biological selectivity of K and Rb (i.e., Rb is not cycled during plant assimilation/release to the same degree as K, Chaudhuri et al., 2007). First, soil K is less abundant than Rb due to < 100% cycling efficiency in soil systems (a "leakage" of plant-cycled K to river runoffs). In addition, Rb^+ is more tightly held by soils than K^+ (Sawhney, 1964), and along the chronosequence, Rb is more enriched than K (based on tau values). Thus, soil K pools may be more intensively cycled in an environment with a greater plant density, producing more prominent plant $\delta^{41}K$ imprints and causing decreases in soil K/Rb ratio due to rapid leaching of mobile plant-cycled K relative to Rb. For example, enhanced tree growth induced faster biogeochemical K cycling and leaching K losses, resulting in lower soil K/Rb ratios (Simonsson et al., 2016). Moreover, crop hydroponic experiments reported preferential ^{39}K uptake from culture solution with $\Delta^{41}K_{solution\text{-}root}$ up to 0.79‰ and $\Delta^{41}K_{solution\text{-}leaf}$ up to 1.57‰ (Christensen et al., 2018), consistent with a recent study on Hawaiian plant $\delta^{41}K$ (Li et al., 2021b). During plant growth, ^{39}K is preferentially taken from soil bioavailable pools by roots, incorporated in root vacuoles, and translocated to aboveground tissues (Christensen et al., 2018). Over time, the inputs of plant-derived K potentially modify soil K isotope composition.

The impact of source mixing on bulk soil $\delta^{41}K$ can be determined based on the proportion of XANES-based mica-K (Table 4), which provides insights into the role of dust accretion. It is known that quartz and mica/illite are uniquely associated with long-distance mineral aerosols accreted on Hawai'i (Rex et al., 1969; Jackson et al., 1971; Porder et al., 2007). As quartz is free of lattice K, the most identifiable K-bearing phase from atmospherically deposited mineral aerosols is mica/illite (Chen et al., 2020). The comparison between soil $\delta^{41}K$ and XANES-based mica-K is provided in Fig. 8a. Previous studies reported that the average composition of mineral aerosols deposited in the Pacific Ocean varied little over the period spanning this chronosequence (Kyte et al., 1993), and Asian dust inputs reflect the average composition of the UCC (Zieman et al., 1995). We infer that $\delta^{41}K$ of mineral aerosols is similar to $\delta^{41}K_{UCC}$ (Huang et al., 2020). With the continuous addition of mineral aerosols, soil $\delta^{41}K$ increases towards the mineral aerosol value estimated from the UCC composition (Fig. 8a). Due to soluble K derived from wet deposition, the continuous inputs of marine aerosols partially balance the leaching loss of K (Kennedy et al. 1998), serving as terrestrial ecosystem nutrients (Chadwick et al., 1999) and thus modifying soil isotopic compositions in Hawai'i (Kurtz et al., 2001; Wiegand

et al., 2005; Chadwick et al., 2009; Ryu et al., 2014; Ryu et al., 2020). Marine aerosol imprints can be assessed by soil $\delta^{41}K$ values due to an isotopic difference of ~0.5‰ between underlying basalts and seawater. In sum, three proxies (hal-K, mica-K, and K/Rb) are used in this study to better understand comparative contributions to $\delta^{41}K$ variation in vertical profiles along this chronosequence.

5.2.2. In-profile K isotope variation

The depth profiles of $\delta^{41}K$ have been shaped to varying degrees by an interplay of (1) basalt weathering and clay formation, (2) plant cycling, and (3) soil source mixing. Except for the youngest soil site, a negative $\delta^{41}K$ excursion from $\delta^{41}K_{Basalt}$ appears at depths of 5–30 cm compared with the $\delta^{41}K$ of soil layers above or below this depth interval (Fig. 5b). Here, we break the soil profiles into three layers (0–5, 5–30, and 30–100 cm, based on the average value of each sampling interval) with distinct isotope patterns and evaluate the processes responsible for the patterns.

In the surface horizons (0–5 cm in depth), soil $\delta^{41}K$ shows both higher and lower values compared to basaltic $\delta^{41}K$ (Fig. 5b). As the substrate age increases from 0.3 to 20 ky, the surface soil $\delta^{41}K$ reaches the minimum (-1.47 ± 0.05‰) of the range of surface soil values along the chronosequence (-1.47 ± 0.05‰ to -0.09 ± 0.08‰). The minimum in $\delta^{41}K$ at 20 ky is paralleled by the highest plant cover (Fig. S1) and greatest soil organic carbon content (Table 1). We argue that these features all suggest high plant productivity, rapid turnover of organic matter, and substantial biological control on $\delta^{41}K$. The surface soil $\delta^{41}K$ values at the 150 and 1,400 ky sites are more positive and closer to seawater $\delta^{41}K$ values (Fig. 5b). The addition of K derived from seawater to soil exchangeable sites (including organic binding ligands) should be substantial (Vitousek, 2004), generating more positive $\delta^{41}K$ in surface soils. Moreover, NaBph4-K derived from clay interlayers shows high $\delta^{41}K$ values (Table 3), revealing ion exchange processes between clay interlayer K^+ and seawater K^+.

In the intermediate-depth horizons (5–30 cm in depth), bulk soil $\delta^{41}K$ values are lower than the basaltic value (i.e., $\Delta^{41}K_{basalt\text{-}soil}$ up to ~2‰, Fig. 5b) and the magnitudes of K isotope fractionation are larger than previously studied weathering profiles (~0.5‰, Chen et al., 2020; Teng et al., 2020). Prominent biological imprints on the middle soil horizons can be supported by a negative correlation between soil K/Rb and $\delta^{41}K$ ($R^2 = 0.79$, Fig. 7b). Low K/Rb and $\delta^{41}K$ can be found in intermediate-aged soil sites (20–1,400 ky) relative to those of the youngest and oldest sites (Fig. 7a), and a sample in the 20 ky site shows the lowest K/Rb ratio (156.6) and $\delta^{41}K$ (-1.32 ± 0.06‰) value. The features agree with the fact that the 20 ky site has the densest tree coverage (Fig. S1) with the highest organic carbon content (Fig. 3a) and humic-K proportion (Fig. 5a), revealing the strongest plant activity. We infer the enrichment of hal-K in the middle depth of the 20 and 150 ky sites (Fig. 6b) likely supports the preservation of plant-cycled K (lighter than basaltic K) in the halloysite interlayers. It is also possible that isotopically light K is fixed in the interlayer space of halloysite. In the youngest site (0.3 ky) with weak weathering, plant-cycled K is minor relative to K derived from basalts and soil $\delta^{41}K$ is similar to basalt $\delta^{41}K$ (Fig. 5b). The older soil sites (>150 ky) exhibit progressive reduction in $\Delta^{41}K$ (between soils and basalts) in the middle depth. This stepwise reduction may be ascribed to a lower biological cycling influence (Fig. S1).

An issue that needs to be addressed is the degree of plant-driven K isotope fractionation in this chronosequence, which is poorly constrained due to a scarcity of plant sampling. It is known that the mechanisms of K isotope fractionation between plants and the sources depend on soil K bioavailability (Christensen et al., 2018). We infer that the fractionation mechanisms are similar along the chronosequence given near-consistent K contents ~0.6% in plant dry-mass (Fig. S5, Mallarino and Higashi, 2009) and no apparent changes in foliar K concentration and no bioavailability limitation (*M. polymorpha*, Fig. S5, Vitousek et al., 1995). Another issue is the discrepancy between the accumulation of organic matter and humic-K in the surface horizons with lower soil $\delta^{41}K$ at the middle horizons, which may be ascribed to the release of highly mobile K^+ during organic matter decomposition at the top moving deeper in the profile. The leaching of plant-cycled K from surface soils by rainfall infiltration is possible and this process has been reported for biologically cycled Ca, Sr, Ba, and Mg in the chronosequence soils (Bullen and Chadwick, 2016; Ryu et al., 2020).

In the deep horizons (30–100 cm in depth), soil $\delta^{41}K$ is lower ($\Delta^{41}K_{basalt\text{-}soil}$ up to 0.3‰, Fig. 5b) compared with basaltic $\delta^{41}K$, and soil $\delta^{41}K$ value increases towards basaltic $\delta^{41}K$ with increasing depth (Fig. 5b). There are no correlations between soil K/Rb and $\delta^{41}K$ values in samples of the deep horizons, and their K/Rb and $\delta^{41}K$ values fall within narrow ranges close to the signal of mineral aerosols (Fig. 7b). Hence, we suggest that biological impacts on soil K budgets are minor in the deep horizons compared to the shallow horizons, and mineral aerosol inputs dominate the deep soil K composition as explained in section 5.1. This interpretation is also supported by the comparison between mica-K and $\delta^{41}K$ (Fig. 8b). Except for the 0.3 ky site, the deep soils are enriched in mica-K (up to 100%) and have $\delta^{41}K$ (-0.70 to -0.46‰, ave. -0.57‰) similar to mineral aerosol $\delta^{41}K$ approximated by $\delta^{41}K_{UCC}$ (ave. -0.44 ± 0.05‰, Huang et al.,2020) relative to shallow soils (Fig. 8b). Again, there is very little K in this layer and what was inherited from basalts is largely leached, therefore there is a small amount of K that is held against leaching in mica lattice and dominants soil K budget.

The vertical patterns of bulk soil $\delta^{41}K$ and $\delta^{41}K_{NH4Ac}$ are similar and $\delta^{41}K_{NH4Ac}$ values are higher than bulk soil $\delta^{41}K$ (Fig. 5b). This feature suggests similar impacts of Earth surface processes on bulk soil K and labile K fractions. To explain the isotopic difference between bulk soil $\delta^{41}K$ and $\delta^{41}K_{NH4Ac}$, two possible mechanisms are proposed. First, preferential plant uptake (Christensen et al., 2018; Li et al., 2021b) of isotopically light K may increase the $\delta^{41}K$ value of soil exchangeable components. Second, in sites older than 0.3 ky, near-complete depletion of basalt K enables the dominance of dust addition, and thus soil exchangeable components are primarily replenished by marine aerosols (Fanning et al., 1989; Wiegand et al., 2005;

Chadwick et al., 2009). It is supported by increasing $\delta^{41}K$ of NH_4Ac-K of subsurface soils to a greater depth, approaching that of modern seawater (~0.14‰, Hille et al., 2019; Wang et al., 2021). It is likely that isotopically heavy, labile K is easily leached by rainfall, thus having little effect on $\delta^{41}K_{Bulk}$. The isotopic fractionation between the bulk soil K and labile K is less in 0.3 ky site compared with the older sites and $\delta^{41}K_{NH4Ac}$ is similar to basalt $\delta^{41}K$. We infer that exchangeable K in the 0.3 ky site is mainly supplied from congruent basalt weathering, masking the imprint of plant cycling, weathering, and atmospheric inputs.

5.3. Comparison to other isotope studies

The chronosequence soil sites reported in this study have been characterized for multiple isotope systems, including Li, Ca, Mg, and Si isotopes (e.g., Ziegler et al., 2005; Wiegand et al., 2005; Ryu et al., 2014; Ryu et al., 2020). Previous studies have investigated the biogeochemical cycles of the elements of interest in soil systems and highlighted the interplays between basalt weathering, atmospheric deposition, and plant cycling. The first major conclusion is the variable rate of the depletion of Li, K, Ca, Mg and Si from the soils. However, the depletion degree of K in the soils is more significant than that of Li and Mg, based on the tau value (Ryu et al., 2014) and K is mostly depleted in all the sites ($\tau_{K,\ Nb}$ of −1.0 to −0.9) except for the youngest site. This elemental pattern may be ascribed to (1) the susceptibility of K-bearing primary components (e.g., feldspars and basaltic glass) to weathering, (2) intense vegetative cycling, and (3) labile association of K with soils due to its exchangeability on the surfaces and incompatibility within clay structures (Eggleton et al., 1987; Li et al., 2021a). Another important conclusion is the biological imprint on bulk soils and exchangeable components, which has been emphasized for K, Ca, Mg, and Si isotopes. As for Li isotopes, plant imprints were not identified because Li is not a nutritive element, and Li isotope values in exchangeable components were not studied in Ryu et al. (2014). However, isotopic variations created by biological cycling vary in depth. Ryu et al. (2020) reported isotopically heavy plant Mg imprints on subsurface soils instead of organic-rich surface soils. Similar to Mg isotope patterns, isotopically light K derived from vegetative decay is prominent in the subsoil at 5–30 cm. As discussed in Section 5.2.2, the leaching of plant K and Mg from surface soils could be important. Isotopically light Mg and heavy K and Ca found in the exchangeable pool of surface soils is likely caused by the mixing of marine aerosols with plant preferential uptake of ^{26}Mg, ^{39}K, and ^{40}Ca (e.g., Wiegand et al., 2005; Ryu et al., 2020; and this study). Nevertheless, it is not the case for Si isotopes that are complicated by phytolith (small silica particles between 5 and 100 μm that form within plants) precipitation, causing low $\delta^{30}Si$ in surface soils (Ziegler et al., 2005).

5.4. Broader implications

Soil development involves weathering of the substrate and microbial modification of dead organic matter. These processes are subject to both leaching losses and additions (from the atmosphere), and the mass balances can be complex. Isotopes can be powerful tools to assist in reconstructing processes, particularly when combined with state-factor analysis (Vitousek, 2004). In this study, we assess the fate of K during soil development on basalts through the use of spectroscopic and isotopic techniques. In brief, $\delta^{41}K$ in the 0.3 ky site keeps near constant and is close to the basaltic value due to the dominance of primary materials. A wide distribution of 20 ky site $\delta^{41}K$ in soil profiles marks the onset of shifts to a more open, leached K cycle in the older soil sites. Leaching loss of K parallel soil development and dramatic reductions in soil $\delta^{41}K$ in the middle depth (10–30 cm) become prominent in sites of 20–150 ky because of strong plant cycling of K, which decreases at the soil sites with increasing age due to forest recession. The depletion of basaltic K and decreases in plant imprints lead to the dominance of atmospheric sources in 1,400–4,100 ky soil sites. In sum, soil $\delta^{41}K$ composition serves as a temporal record of biogeochemical activity.

Plant cycling with preferential uptake of ^{39}K agrees with the report of crop hydroponic experiments and natural plant studies (Li, 2017; Christensen et al., 2018; Li et al., 2021b). Observed impacts of plant activity on K in soils correspond well to the forest coverage and soil organic carbon content at each sampling site (Figs. S1 and 3a). There is a vertical difference between the lowest soil $\delta^{41}K$ value and the enrichment of organic matter in soil profiles due to downward leaching of plant-derived light K. Importantly, a wide K isotope variation in terrestrial records is not necessarily linked with extreme weathering, calling for cautions. Isotopic fractionation of K driven by processes such as chemical weathering, and biological cycling may be a useful tracer of terrestrial processes. For example, glacial-interglacial cycles may affect the relative dominance of chemical and physical weathering and cause the variation in precipitation and biological productivity that may affect the $\delta^{41}K$ value in paleosols. It is known that soils cannot be the ultimate sink of light K required to balance high river $\delta^{41}K$ values and fluvial and marine sediments are likely the final storage reservoir of K. These changes may further modulate riverine inputs, where there is a high likelihood that sedimentary records will archive changes. Therefore, it is significant for the K isotope composition of rivers draining silicate rocks and continental margin sediments. Future work on $\delta^{41}K$ signals in sedimentary archives is needed to examine this hypothesis.

6. CONCLUSIONS

This Hawaiian chronosequence allows us to investigate the influence of soil age on soil K isotope composition. Combining geochemical analysis with spectroscopic techniques, we report the K isotope composition in soil chronosequence developed over 4-million-year history. Overall, changes in soil [K] and $\delta^{41}K$ emphasize interplays between chemical weathering, biological cycling, and source mixing with extraneous materials (mineral and marine aerosols). The first two processes preferentially retain isotopically light K in soils. Source mixing with mineral and

marine aerosols introduces isotopically comparable to or heavier K than parent basalts into soils, respectively. Seawater-sourced K is particularly critical for soil exchangeable component because of the replenishment of marine aerosols via rainfall. Compared to element data, K isotope variations in Hawaiian chronosequence soils offer valuable insights into the biotic and abiotic cycles of K during soil development.

DECLARATION OF COMPETING INTEREST

The authors declare that they have no known competing financial interests or personal relationships that could have appeared to influence the work reported in this paper.

ACKNOWLEDGMENTS

The authors acknowledge the funding support from the NSF Career Award (EAR-1848153) to X.-M. Liu, and the Martin Research Fellowship from UNC-CH and GSA research award to W. Li. We thank Weiqiang Li and Jeffrey Catalano for editorial handling and five anonymous reviewers, whose constructive comments significantly improve the paper. We thank Xikai Wang, Mohsen Shakouri and Jing Sun for XAFS measurement, processing, and fruitful discussion. The K *K*-edge XANES spectra provided in this study were collected at Canadian Light Source (CLS), with the approval of CLS proposal review committee (No. 30G09959, 30GU10898 and 32GU010898). Canadian Light Source is supported by Canada Foundation for Innovation, Natural Sciences & Engineering Research Council of Canada, University of Saskatchewan, Government of Saskatchewan, Western Economic Diversification Canada, National Research Council Canada, and Canadian Institutes of Health Research. Some of the K *K*-edge XANES spectra were also collected in Photon Factory (PF; Tsukuba, Japan) with the approval of PF (Proposal No. 2022G126).

Appendix A. Supplementary material

Supplementary material to this article can be found online at https://doi.org/10.1016/j.gca.2022.06.025.

REFERENCES

An S., Luo X. and Li W. (2022) Precise measurement of 41K/39K ratios by HR-MC-ICP-MS under a dry and hot plasma setting. *Rapid Commun. Mass Spectrom.*, e9289–e9289.

Arendt C. A., Aciego S. M. and Hetland E. A. (2015) An open source Bayesian Monte Carlo isotope mixing model with applications in Earth surface processes. *Geochem. Geophy. Geosy.* **16**, 1274–1292.

Arnold P. W. (1960) Nature and mode of weathering of soil-potassium reserves. *J. Sci. Food Agric.* **11**(6), 285–292.

Bargrizan S., Smernik R. J. and Mosley L. M. (2017) Development of a spectrophotometric method for determining pH of soil extracts and comparison with glass electrode measurements. *Soil Sci. Soc. Am. J.* **81**, 1350–1358.

Brimhall G. H. and Dietrich W. E. (1987) Constitutive mass balance relations between chemical composition, volume, density, porosity, and strain in metasomatic hydrochemical systems: results on weathering and pedogenesis. *Geochim. Cosmochim. Acta* **51**, 567–587.

Blakemore L. C. (1987) Methods for chemical analysis of soils. *NZ Soil Bureau Sci. Rep.* **80**, 72–76.

Bullen T. and Chadwick O. (2016) Ca, Sr and Ba stable isotopes reveal the fate of soil nutrients along a tropical climosequence in Hawaii. *Chem. Geol.* **422**, 25–45.

Calvin S. (2013) *XAFS for Everyone*. CRC Press, Boca Raton, FL, USA.

Chadwick O. A., Derry L. A., Vitousek P. M., Huebert B. J. and Hedin L. O. (1999) Changing sources of nutrients during four million years of ecosystem development. *Nature* **397**, 491–497.

Chadwick O. A. and Chorover J. (2001) The chemistry of pedogenic thresholds. *Geoderma* **100**, 321–353.

Carrillo J. H., Hastings M. G., Sigman D. M. and Huebert B. J. (2002) Atmospheric deposition of inorganic and organic nitrogen and base cations in Hawaii. *Glob. Biogeochem. Cycles* **16**, 1076.

Chadwick O. A., Brimhall G. H. and Hendricks D. M. (1990) From a black to a gray box—a mass balance interpretation of pedogenesis. *Geomorphology* **3**, 369–390.

Chadwick O. A., Kelly E. F., Hotchkiss S. C. and Vitousek P. M. (2007) Precontact vegetation and soil nutrient status in the shadow of Kohala Volcano, Hawaii. *Geomorphology* **89**, 70–83.

Chadwick O. A., Gavenda R. T., Kelly E. F., Ziegler K., Olson C. G., Crawford Elliott W. and Hendricks D. M. (2003) The impact of climate on the biogeochemical functioning of volcanic soils. *Chem. Geol.* **202**, 195–223.

Chadwick O. A., Derry L. A., Bern C. R. and Vitousek P. M. (2009) Changing sources of strontium to soils and ecosystems across the Hawaiian Islands. *Chem. Geol.* **267**, 64–76.

Chadwick O. A., Chorover J., Chadwick K. D., Bateman J. B., Slessarev E. W., Kramer M., Thompson A. and Vitousek P. M. (2020) Soil Development within the Hawaiian Time-Climate Matrix. In *Biogeochemistry in the Critical Zone* (eds. A. Waymore and J. Chorover). Springer/Nature Press, pp. 378–398.

Chaudhuri S., Clauer N. and Semhi K. (2007) Plant decay as a major control of river dissolved potassium: A first estimate. *Chem. Geol.* **243**, 178–190.

Chen H., Tian Z., Tuller-Ross B., Korotev R. L. and Wang K. (2019) High-precision potassium isotopic analysis by MC-ICP-MS: An inter-laboratory comparison and refined K atomic weight. *J. Anal. At. Spectrom.* **34**, 160–171.

Chen H., Liu X. M. and Wang K. (2020) Potassium isotope fractionation during chemical weathering of basalts. *Earth Planet. Sci. Lett.* **539**.

Chorover J., DiChiaro M. J. and Chadwick O. A. (1999) Structural charge and cesium retention in a chronosequence of tephritic soils. *Soil Sci. Soc. Am. J.* **63**, 169–177.

Chorover J., Amistadi M. K. and Chadwick O. A. (2004) Surface charge evolution of mineral-organic complexes during pedogenesis in Hawaiian basalt. *Geochim. Cosmochim. Acta* **68**, 4859–4876.

Christensen J. N., Qin L., Brown S. T. and Depaolo D. J. (2018) Potassium and Calcium Isotopic Fractionation by Plants (Soybean [Glycine max], Rice [Oryza sativa], and Wheat [Triticum aestivum]). *ACS Earth Space Chem.* **2**, 745–752.

Cox A. E., Joern B. C., Brouder S. M. and Gao D. (1999) Plant-available potassium assessment with a modified sodium tetraphenylboron method. *Soil Sci. Soc. Am. J.* **63**, 902–911.

Crews T. E., Kitayama K., Fownes J. H., Riley R. H., Herbert D. A., Mueller-Dombois D. and Vitousek P. M. (1995) Changes in soil phosphorus fractions and ecosystem dynamics across a long chronosequence in Hawaii. *Ecology* **76**, 1407–1424.

Eggleton R. A., Foudoulis C. and Varkevisser D. (1987) Weathering of basalt: changes in rock chemistry and mineralogy. *Clays Clay Miner.* **35**, 161–169.

Eriksson E. (1957) The chemical composition of Hawaiian rainfall. *Tellus* **9**, 509–520.

Fanning D. S., Keramidas V. Z. and El-Desoky M. A. (1989) Micas. In *Minerals in soil environments* (eds. J. B. Dixon and S. B. Weed). Soil Science Society of America, Madison, Wisconsin, USA, pp. 551–634.

Goodfellow B. W., Chadwick O. A. and Hilley G. E. (2014) Depth and character of rock weathering across a basaltic-hosted climosequence on Hawai'i. *Earth Surf. Process. Landf.* **39**, 381–398.

Han H. S. and Lee K. D. (2005) Phosphate and potassium solubilizing bacteria effect on mineral uptake, soil availability and growth of eggplant. *Res. J. Agric. Biol. Sci.* **1**, 176–180.

Helfenstein J., Tamburini F., von Sperber C., Massey M. S., Pistocchi C., Chadwick Peter Vitousek O. A., Kretzschmar R. and Frossard E. (2018) Combining spectroscopic and isotopic techniques gives a dynamic view of phosphorus cycling in soil. *Nat. Commun.* **9**, 1–9.

Hille M., Hu Y., Huang T. Y. and Teng F. Z. (2019) Homogeneous and heavy potassium isotopic composition of global oceans. *Sci. Bull.* **64**(23), 1740–1742.

Hotchkiss S., Vitousek P. M., Chadwick O. A. and Price J. (2000) Climate cycles, geomorphological change, and the interpretation of soil and ecosystem development. *Ecosystems* **3**, 522–533.

Hu Y., Chen X. Y., Xu Y. K. and Teng F. Z. (2018) High-precision analysis of potassium isotopes by HR-MC-ICPMS. *Chem. Geol.* **493**, 100–108.

Hu Y. F., Coulthard I., Chevrier D., Wright G., Igarashi R., Sitnikov A., Yates B. W., Hallin E. L., Sham T. K. and Reininger R. (2010) Preliminary commissioning and performance of the soft x-ray micro-characterization beamline at the Canadian light source. *AIP Conf. Proc.* **1234**, 343–346.

Huang T. Y., Teng F. Z., Rudnick R. L., Chen X. Y., Hu Y., Liu Y. S. and Wu F. Y. (2020) Heterogeneous potassium isotopic composition of the upper continental crust. *Geochim. Cosmochim. Acta* **278**, 122–136.

Jackson M. L., Levelt T. W. M., Syers J. K., Rex R. W., Clayton R. N., Sherman G. D. and Ueharam G. (1971) Geomorphological relationships of tropospherically derived quartz in the soils of the Hawaiian Islands. *Soil Sci. Soc. Am. J.* **35**, 515–525.

Kennedy M. J., Chadwick O. A., Vitousek P. M., Derry L. A. and Hendricks D. M. (1998) Changing sources of base cations during ecosystem development, Hawaiian Islands. *Geology* **26**, 1015–1018.

Kurtz A. C., Derry L. A., Chadwick O. A. and Alfano M. J. (2000) Refractory element mobility in volcanic soils. *Geology* **28**, 683–686.

Kurtz Andrew C., Derry L. A. and Chadwick O. A. (2001) Accretion of Asian dust to Hawaiian soils: Isotopic, elemental, and mineral mass balances. *Geochim. Cosmochim. Acta* **65**, 1971–1983.

Kyte F. T., Leinen M., Heath G. R. and Zhou L. (1993) Cenozoic sedimentation history of the central North Pacific: Inferences from the elemental geochemistry of core LL44-GPC3. *Geochim. Cosmochim. Acta* **57**, 1719–1740.

Lenton T. M. and Von Bloh W. (2001) Biotic feedback extends the life span of the biosphere. *Geophys. Res. Lett.* **28**, 1715–1718.

Lynch H. B., Epps K. Y., Fukami T. and Vitousek P. M. (2012) Introduced canopy tree species effect on the soil microbial community in a montane tropical forest. *Pac. Sci.* **66**, 141–150.

Li S., Li W., Beard B. L., Raymo M. E., Wang X., Chen Y. and Chen J. (2019) K isotopes as a tracer for continental weathering and geological K cycling. *Proc. Natl. Acad. Sci. U. S. A.* **116**, 8740–8745.

Li W., Beard B. L. and Li S. (2016) Precise measurement of stable potassium isotope ratios using a single focusing collision cell multi-collector ICP-MS. *J. Anal. At. Spectrom.* **31**, 1023–1029.

Li W. (2017) Vital effects of K isotope fractionation in organisms: observations and a hypothesis. *Acta Geochimica* **36**, 374–378.

Li W., Liu X. M. and Hu Y. (2020) Potassium and Calcium K-Edge XANES in Chemical Compounds and Minerals: Implications for Geological Phase Identification. *Geostand. Geoanalytical Res.* **44**, 805–819.

Li W., Liu X. M., Hu Y., Teng F. Z. and Hu Y. (2021a) Potassium isotopic fractionation during clay adsorption. *Geochim. Cosmochim. Acta* **304**, 160–177.

Li W., Liu X. M., Hu Y., Teng F. Z., Hu Y. F. and Chadwick O. A. (2021b) Potassium isotopic fractionation in a humid and an arid soil–plant system in Hawai 'i. *Geoderma* **400**.

Li W., Liu X. M., Wang K. and Koefoed P. (2021c) Lithium and potassium isotope fractionation during silicate rock dissolution: An experimental approach. *Chem. Geol.* **568**.

Li X., Han G., Zhang Q. and Miao Z. (2020) An optimal separation method for high-precision K isotope analysis by using MC-ICP-MS with a dummy bucket. *J. Anal. At. Spectrom.* **35**, 1330–1339.

Lucas Y. (2001) The role of plants in controlling rates and products of weathering: importance of biological pumping. *Annu. Rev. Earth Planet. Sci.* **29**, 135–163.

Mallarino A. P. and Higashi S. L. (2009) Assessment of potassium supply for corn by analysis of plant parts. *Soil Sci. Soc. Am. J.* **73**, 2177–2183.

Morgan L. E., Santiago Ramos D. P., Davidheiser-Kroll B., Faithfull J., Lloyd N. S., Ellam R. M. and Higgins J. A. (2018) High-precision 41K/39K measurements by MC-ICP-MS indicate terrestrial variability of: δ41K. *J. Anal. At. Spectrom.* **33**, 175–186.

Ndayiragije S. and Delvaux B. (2004) Selective sorption of potassium in a weathering sequence of volcanic ash soils from Guadeloupe, French West Indies. *Catena* **56**, 185–198.

Nesbitt H. and Young G. M. (1982) Early Proterozoic climates and plate motions inferred from major element chemistry of lutites. *Nature* **299**, 715–717.

Porder S., Hilley G. E. and Chadwick O. A. (2007) Chemical weathering, mass loss, and dust inputs across a climate by time matrix in the Hawaiian Islands. *Earth Planet. Sci. Lett.* **258**, 414–427.

Pett-Ridge J. C., Monastra V. M., Derry L. A. and Chadwick O. A. (2007) Importance of atmospheric inputs and Fe-oxides in controlling soil uranium budgets and behavior along a Hawaiian chronosequence. *Chem. Geol.* **244**, 691–707.

Quantin P., Gautheyrou J. and Lorenzoni P. (1988) Halloysite formation through in situ weathering of volcanic glass from trachytic pumices, Vico's Volcano. *Italy. Clay Miner.* **23**, 423–437.

Ravel B. and Newville M. (2005) ATHENA, ARTEMIS, HEPHAESTUS: Data analysis for X-ray absorption spectroscopy using IFEFFIT. *J. Synchrotron Radiat.* **12**, 537–541.

Rex R. W., Syers J. K., Jackson M. L. and Clayton R. N. (1969) Eolian origin of quartz in soils of Hawaiian Islands and in Pacific pelagic sediments. *Science* **163**, 277–279.

Rudnick R. L. and Gao S. (2013) Composition of the Continental Crust. In *Treatise on Geochemistry*. Second Edition Elsevier Inc., pp. 1–51.

Ryu J. S., Vigier N., Lee S. W., Lee K. S. and Chadwick O. A. (2014) Variation of lithium isotope geochemistry during basalt weathering and secondary mineral transformations in Hawaii. *Geochim. Cosmochim. Acta* **145**, 103–115.

Ryu J. S., Vigier N., Derry L. and Chadwick O. A. (2020) Variations of Mg isotope geochemistry in soils over a Hawaiian 4 Myr chronosequence. *Geochim. Cosmochim. Acta* **292**, 94–114.

Sardans J. and Peñuelas J. (2015) Potassium: A neglected nutrient in global change. *Glob. Ecol. Biogeogr.* **24**, 261–275.

Sawhney B. L. (1964) Sorption and fixation of microquantities of cesium by clay minerals: effect of saturating cations. *Soil Sci. Soc. Am. J.* **28**, 183–186.

Santiago Ramos D. P., Coogan L. A., Murphy J. G. and Higgins J. A. (2020) Low-temperature oceanic crust alteration and the isotopic budgets of potassium and magnesium in seawater. *Earth Planet. Sci. Lett.* **541**.

Soil Survey Laboratory Staff (2004) *Soil Survey Laboratory Methods Manual* Soil Survey Investigations Report. USDA-SCS, Washington DC.

Soil Survey Staff (2017) *Soil Survey Manual Agriculture. Handbook 18*. USDA, Natural Resources Conservation Service.

Spengler S. R. and Garcia M. O. (1988) Geochemistry of the Hawi lavas, Kohala Volcano. *Hawaii. Contrib. Mineral. Petrol.* **99**, 90–104.

Simonsson M., Bergholm J., Lemarchand D. and Hillier S. (2016) Mineralogy and biogeochemistry of potassium in the Skogaby experimental forest, southwest Sweden: pools, fluxes and K/Rb ratios in soil andbiomass. *Biogeochemistry* **131**, 77–102.

Singh B. and Grafe M. (2010) *Synchrotron-based techniques in soils and sediments*. Elsevier, Burlington, USA, Amsterdam, The Netherlands, Oxford United Kingdom.

Stewart B. W., Capo R. C. and Chadwick O. A. (2001) Effects of rainfall on weathering rate, base cation provenance, and Sr isotope composition of Hawaiian soils. *Geochim. Cosmochim. Acta* **65**, 1087–1099.

Takahashi T., Dahlgren R. A., Theng B. K. G., Whitton J. S. and Soma M. (2001) Potassium-selective, halloysite-rich soils formed in volcanic materials from northern California. *Soil Sci. Soc. Am. J.* **65**, 516–526.

Takahashi Y., Dahlgren R. A., Kanno H., Nanzyo M. and Takahashi T. (2018) Mechanisms for high potassium selectivity of soils dominated by halloysite from northern California, USA. *J. Soil Sci. Plant Nutr.* **64**, 90–99.

Teng F. Z., Dauphas N. and Watkins J. M. (2017) Non-Traditional Stable Isotopes: Retrospective and Prospective. *Rev. Mineral. Geochem.* **82**, 1–26.

Teng F. Z., Hu Y., Ma J. L., Wei G. J. and Rudnick R. L. (2020) Potassium isotope fractionation during continental weathering and implications for global K isotopic balance. *Geochim. Cosmochim. Acta* **278**, 261–271.

Thompson A., Ruiz J., Chadwick O. A., Titus M. and Chorover J. (2007) Rayleigh fractionation of iron isotopes during pedogenesis along a climate sequence of Hawaiian basalt. *Chem. Geol.* **238**, 72–83.

Torn M. S., Trumbore S. E., Chadwick O. A., Vitousek P. M. and Hendricks D. M. (1997) Mineral control of soil organic carbon storage and turnover. *Nature* **389**, 170–173.

Tripler C. E., Kaushal S. S., Likens G. E. and Todd Walter M. (2006) Patterns in potassium dynamics in forest ecosystems. *Eco. Lett.* **9**, 451–466.

Uhlig D., Amelung W. and von Blanckenburg F. (2020) Mineral nutrients sourced in deep regolith sustain long-term nutrition of mountainous temperate forest ecosystems. *Global Biogeochem. Cy.* **34**, e2019GB006513.

Vitousek P. M. (2004) *Nutrient Cycling and Limiitation: Hawaii as a Model System*. Princeton University Press, Princeton.

Vitousek P. M., Turner D. R. and Kitayama K. (1995) Foliar nutrients during long-term soil development in Hawaiian montane rain forest. *Ecology* **76**, 712–720.

Vitousek P. M., Chadwick O. A., Crews T. E., Fownes J. H., Hendricks D. M. and Herbert D. (1997) Soil and ecosystem development across the Hawaiian Islands. *GSA Today* **7**, ISSN: 10525173.

Vitousek P. M., Kennedy M. J., Derry L. A. and Chadwick O. A. (1999) Weathering versus atmospheric sources of strontium in ecosystems on young volcanic soils. *Oecologia* **121**, 255–259.

Wang K. and Jacobsen S. B. (2016) An estimate of the Bulk Silicate Earth potassium isotopic composition based on MC-ICPMS measurements of basalts. *Geochim. Cosmochim. Acta* **178**, 223–232.

Wang K., Close H. G., Tuller-Ross B. and Chen H. (2020) Global Average Potassium Isotope Composition of Modern Seawater. *ACS Earth Space Chem.* **4**, 1010–1017.

Wang K., Peucker-Ehrenbrink B., Chen H., Lee H. and Hasenmueller E. A. (2021) Dissolved potassium isotopic composition of major world rivers. *Geochim. Cosmochim. Acta* **294**, 145–159.

Wardle D. A., Walker L. R. and Bardgett R. D. (2004) Ecosystem properties and forest decline in contrasting long-term chronosequences. *Science* **305**, 509–513.

Wiegand B. A., Chadwick O. A., Vitousek P. M. and Wooden J. L. (2005) Ca cycling and isotopic fluxes in forested ecosystems in Hawaii. *Geophys. Res. Lett.* **32**, 1–4.

Xu Y. K., Hu Y., Chen X. Y., Huang T. Y., Sletten R. S., Zhu D. and Teng F. Z. (2019) Potassium isotopic compositions of international geological reference materials. *Chem. Geol.* **513**, 101–107.

Zheng, X.Y., Chen, X.Y., Ding, W., Zhang, Y., Charin, S. and Gérard, Y. (2022). High precision analysis of stable potassium (K) isotopes by the collision cell MC-ICP-MS "Sapphire" and a correction method for concentration mismatch. J. Anal. At. Spectrom. (in press) DOI: 10.1039/D2JA00078D.

Ziegler K., Chadwick O. A., Brzezinski M. A. and Kelly E. F. (2005) Natural variations of δ^{30}Si ratios during progressive basalt weathering, Hawaiian Islands. *Geochim. Cosmochim. Acta* **69**, 4597–4610.

Zieman J. J., Holmes J. L., Connor D., Jensen C. R., Zoller W. H., Hermann D. M., Parrington J. R. and Gordon G. E. (1995) Atmospheric aerosol trace element chemistry at Mauna Loa Observatory: 1. 1979–1985. *J. Geophys. Res. Atmos.* **100**, 25979–25994.

Associate editor: Weiqiang Li